Upgrading the small strength tester to test thin silica fibers material properties and calculate the Young's modulus

Erin Momany

August 1, 2017

Student at University of Minnesota

Advisers: Dr. Giles Hammond, Dr. Alan Cumming, and Karl Toland

Institute for Gravitational Research, University of Glasgow

University of Florida International Research Experience for Undergraduates Program

August 1st, 2017

Abstract

Understanding the material properties of thin silica fibers used in the suspension systems of the ground based interferometer gravitational wave detectors is one of the ongoing research topics in the International Gravitational Wave Research program at the University of Glasgow. Young's modulus is a material property that is used in calculations for the suspension thermal noise. The suspension thermal noise includes the noise from: thermoelastic loss, dissipation dilution, and the pendulum loss. One of the topics of investigation is Young's modulus of the silica fibers when the diameter is very small. This report covers the summer internship project to upgrade the existing MKIII small strength testing machine used to on the small silica fibers. Mechanical, hardware, and software improvement were made in order to reduce some of the measurement error. Two fibers were successfully tested once the improvements were made. The breaking force for fiber 1 was measured at .004 $\pm$.0001 N and the breaking force for fiber 2 was .137 $\pm$.0003 N. Fiber 1 breaking stress was calculated at 3.012 $\pm$.151 GPa and fiber 2 breaking stress was 2.637 $\pm$.132 GPa. The Young's modulus for fiber 1 was much lower than fiber 2, where fiber one was calculated at 28 $\pm$6.72 GPa and fiber 2 was calculated to be 84 $\pm$20.16 GPa. The improvement and tests are described in this report along with future work to be done to better understand Young's modulus for thin fibers.

Contents

1 Introduction

1.1 Gravitational Waves

In 1915 Albert Einstein finalized his formulation of the field equations of general relativity; a year later he predicted the existence of gravitational waves [1]. He proposed that gravitational waves are ripples in space-time. Space-time is a mathematical model that relates the three-dimension of space and the one-dimension of time into a single four-dimensional continuum [2]. He proposed that gravitational waves are a result of large energetic processes such as colliding black holes. One hundred years later on September 14th, 2015, Einstein's predictions were confirmed with the first direct detection of gravitational waves at the Hanford, Washington and Livingston, Louisiana LIGO detectors [3]. This opened the doors to a brand new type of astronomy that isn't based on electromagnetic waves and instead is based in gravitational waves.

1.2 Gravitational Wave Detection

Gravitational waves travel at the speed of light while they stretch and compress space-time. In order to detect gravitational waves, the detector has to be sensitive to changes in distance in the order of 10^{-19} meters, which is roughly 1/10,000th the diameter of a proton [4, 5]. Experiments to detect gravitational waves began with physicist Joseph Weber and his resonant mass detectors in the 1960's [6]. Interferometric detectors were first suggested in the early 1960's and 70's [7]. By the early 2000's a set of initial detectors were completed including the TAMA 300 in Japan, GEO 600 in Germany, Virgo in Italy and the two Laser Interferometer Gravitational-wave Observatories (LIGO) in The United States [8].

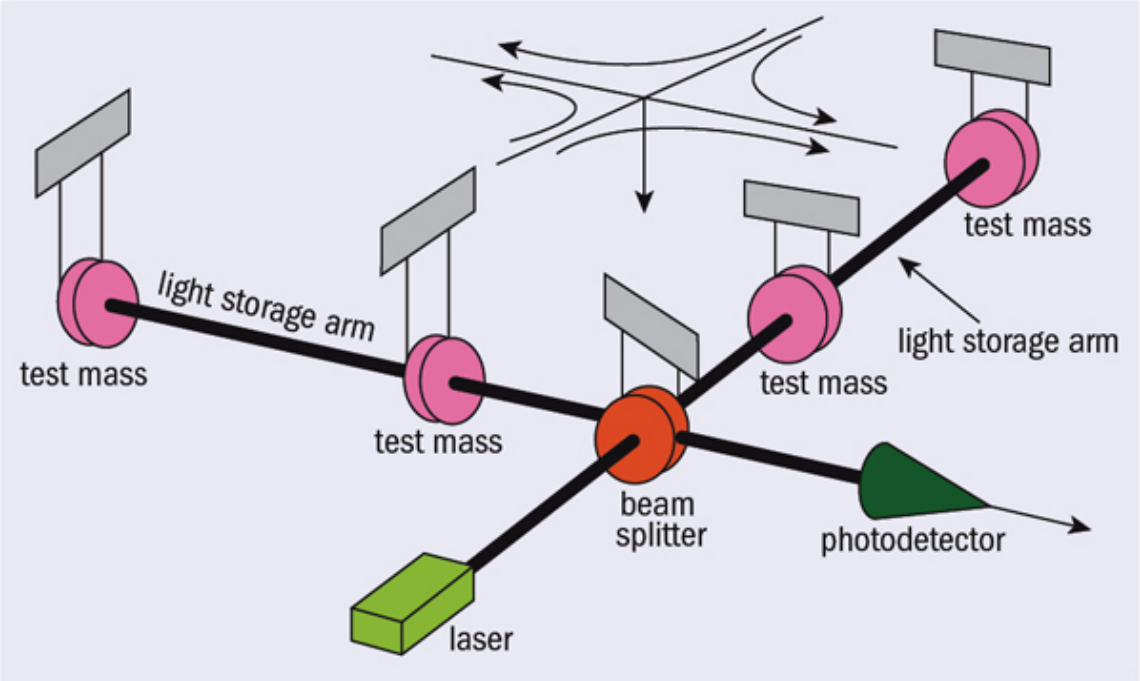

Figure 1.1: Simple diagram of the ground based Interferometer [7]

The detectors have to be very precise in order to detect such small changes. The current method of gravitational wave detection is an advanced version of the Michelson Interferometer. This method uses the fact that light travels at a constant speed and can be used as the "ruler" within the interferometers. The design of the LIGO detectors includes two 4 km arms that stretch out 90 degrees from each other. A laser points down the middle of one of the arms and is split at the intersection by a beam splitter where it then travels down each arm as seen in figure 1.1. This design utilizes Fabry-Perot Cavities and delay lines which are used in the arms of the detectors [4, 9]. Fabry-Perot Cavities are spaces in the arms of the interferometers that use highly reflective mirrors to amplify the laser [4]. They are locked through the use of a control system at a resonance where the length of the cavity is an integral number of the wavelength of the laser to allow the energy in the cavity to build up [4]. The delay lines use a series of mirrors to reflect the beams back and forth which increases the time the beam is in the arm before it reaches the photo-diode for detection. This increases how effective the length of the arms are and allows for a reasonable length of the arm in order to detect the waves in a ground based interferometer. Theoretically, because the laser beams in each arm have traveled the same distance and speed, they should destructively interfere. If there is no gravitational wave then no light should reach the photo-detector. When a gravitational wave passes through the detector then there is no observed complete destructive interference when the beams recombine at the elbow. If a gravitational wave passes through the interferometer, one arm will be stretched and the other will be compressed, then the opposite will happen which results in an oscillatory sequence of observed compressions and expansions [4].

1.3 Suspension Systems

The test masses that the laser passes through and the mirror that reflects the laser are suspended in order to control and reduce seismic noise in the detector. To reduce the thermal noise in these suspension systems a quasi-monolithic design is used with fused silica fibers suspending the test masses and mirrors [10]. It is crucial for the suspension system's design to reduce the thermal displacement noise in order to be able to detect gravitational waves. Suspension thermal noise's operating frequency is approximately 10 to 30 Hz as seen in figure 1.3 below [11]. It is a result from a combination of thermoelastic damping, surface loss, and bulk loss associated with the suspension fiber and weld loss from their attachments.

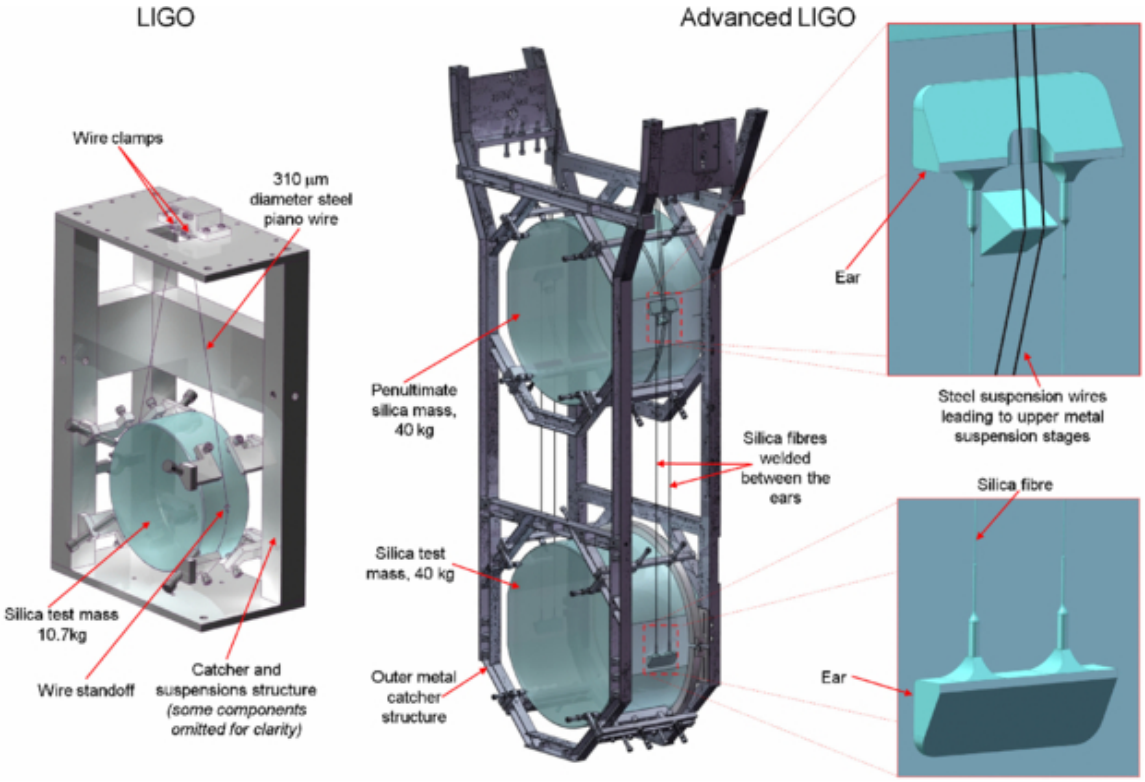

Figure 1.2: Comparison of the initial LIGO (left) steel wire loop suspension and the advanced LIGO monolithic fused silica suspension stage (right), with monolithic section comprising the lower two masses (and suspension fibers) of a four-stage system. Close up images show details of the fused silica attachment ears, silica fibers and suspension wires that suspend this lower monolithic section from the upper stages [12].

1.4 Noise

One of the biggest challenges that limit the sensitivity of the detectors is the noise that can occur from various sources: quantum noise, seismic noise, gravity gradient that produces noise, suspension

thermal noise and other sources. Each of these sources contributes to the total sensitivity limit, depicted by the black line in Figure 1.3. Characterizing these noise sources is required in order to reduce them and increase the ability to detect the gravitational waves.

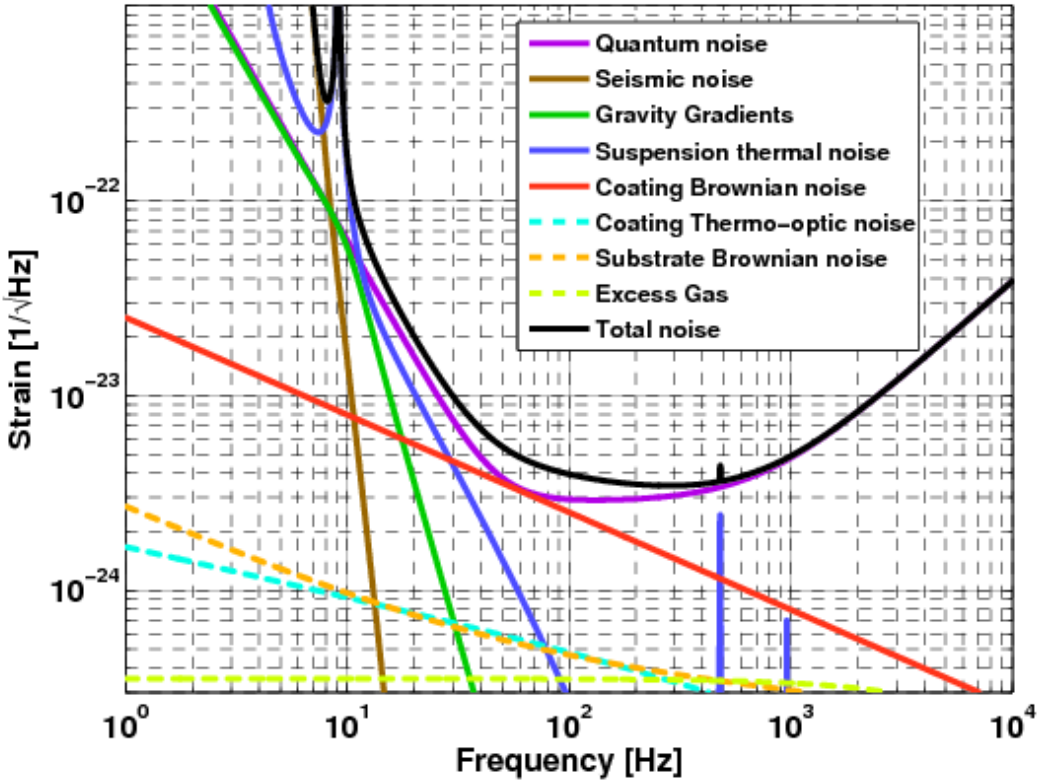

Figure 1.3: The difference noise sources limiting sensitivity of aLIGO over a range of frequencies[11].

1.5 Suspension Thermal Noise

Suspension thermal noise results from the test masses and their suspension systems. Thermal noise comes from the internal vibration in the test masses and internal fluctuation within the suspension fibers due to the thermal energy within the material. Reducing the thermal noise has been key to increasing the ability to detect gravitational waves at low frequencies. This is because the thermal noise dominates at frequencies equal to or below 100 Hz and also peaks in certain high frequencies as a result of the resonant modes of the mirror and violin modes of the suspension [11].

Suspension thermal noise can be organized into external or internal thermal noise. The external category includes the loss of energy in the form of thermal noise to the surrounding environment, which is controlled by a complex environmental control system. The internal thermal noise includes the energy being lost internally in the suspension system in the form of thermal energy [4]. The internal suspension thermal noise is minimized by the intelligent mechanical design of the suspension

stage and choice of very high purity, low dissipation glass compounds for the test masses [12].

In this report, I'll focus on the three different types of internal thermal noise utilize Young's modulus material property in order to calculate them: thermoelastic loss, dissipation dilution, and violin mode.

1.5.1 Thermoelastic Loss

Thermoelastic loss noise is produced through internal dissipation that occurs in the test masses and the suspension. In the suspension, when the silica fiber bends, it creates a temperature gradient that generates a heat flow according to the bending shape and results in a temperature increase where the fiber is compressed and temperature decrease where it's being stretched [4]. This temperature gradient can be calculated using the thermal expansion coefficient [4], α :

$$\alpha = \frac{1}{l}\frac{\Delta l}{\Delta T} \tag{1.1}$$

Where l is the length of the fiber, Δl is the change in length and ΔT is the change in temperature. The equation to calculate the thermoelastic loss includes Young's modulus of the material and can be shown as:

$$\phi_{Thermoelastic} = \frac{YT}{\rho C}\alpha^2 \left(\frac{\omega\tau}{1+\omega^2\tau^2}\right) \tag{1.2}$$

Where $\phi T_{hermoelastic}$ is the linear thermoelastic loss, Y is Young's modulus, T is the temperature, $\rho$is the density of the material, C is the specific heat capacity, ω is the angular frequency, and τ is the characteristic time for heat to flow across the sample [4].The characteristic time for heat flow for a fiber can be calculated by [4]:

$$\tau = \frac{\rho C d^2}{13.55k} \tag{1.3}$$

Where d is the diameter of the fiber.

Research has shown that the thermoelastic noise can be theoretically nullified by the addition of a specific stress on the silica fiber, which is a result of Young's modulus of silica increasing with temperature [13]. To solve for the thermoelastic loss of a silica fiber the equation is [4]:

$$\phi_{ThermoelasticSF} = \frac{Y_o T}{\rho C}\left(\alpha - \alpha_o \frac{\beta}{Y_o}\right)^2 \left(\frac{\omega\tau}{1+\omega^2\tau^2}\right) \tag{1.4}$$

Where the Y_o is Young's modulus at room temperature, α_o is the static stress on each fiber, and all the other variables are the same as from the prior definition of thermoelastic loss. The thermoelastic loss for silica fibers can be canceled out when $\alpha_o = \frac{\alpha\gamma}{\beta}$ [4]. It was discovered that most of the thermoelastic energy in the silica fibers for a LIGO is contained in the 800μm region and if a stress of 195 MPa is applied this noise will be nullified specifically in the aLIGO configuration [4, 13]. Theoretically, this can also be applied to other detectors based off of their specific configurations.

1.5.2 Dissipation Dilution

Gravitational wave detectors use multiple stage pendulum systems to help reduce seismic and thermal noise which means that most of the test mass's energy is in the form of gravitational potential energy [4]. Since most of the energy of the system is contained as gravitational potential and the gravitational field is lossless, only a small amount of the systems total energy is exposed as noise in the system and contributes to the noise that interferes with the ability to detect gravitational waves [9].

The test masses and the fibers used in the suspension are made of fused silica, chosen because it's a low loss material which means it has a high Q factor, a dimensionless parameter in physics that describes the strength of the damping of its oscillations is relative to the width [14]. There is a concentration of energy located at the resonate modes which mean there is less resonance thermal noise [4].

The pendulum mode thermal noise is a result of the mechanical loss associated with the materials that are used in the suspension systems for the tests masses. The Young's modulus of the material is used in this equation to calculate the energy loss due to pendulum mode [4].

$$\phi_{pendulumloss} \approx \phi_{fiberloss} \frac{n\sqrt{TYI}}{2mgL} \tag{1.5}$$

Where $\phi_{fiberloss}$ is the energy stored in the fiber, n is the number of fibers, T is the tension of the fiber, Y is Young's modulus, I is the mass moment of inertia of the fiber, mg is the gravitational field, and L is the length of the fiber. Understanding Young's modulus of the thin silica fibers means that the calculations for these noise sources can be accurately modeled [4].

1.5.3 Violin Mode

The suspension fibers that hold up the test masses also experience a transverse vibrational mode, known as violin modes. These modes are a harmonic series with a number of modes observed depending on how wide the frequency band of the gravitational wave detector is. The loss of energy due to violin mode can be modeled [4]:

$$\phi_{violinloss} = 2\phi_{pendulumloss} \tag{1.6}$$

The theoretical dilution factor of the first violin mode is half that of the pendulum mode. A result of the suspension systems being made from fused silica is that the observed thermal noise associated with the violin modes will be concentrated within a narrow frequency range next to the resonance frequencies. The low loss and high Q for the fused silica results in a long ring-down time of these modes so a damping system is in place in order to limit the downtime of the interferometers [15][16].

1.6 Young's Modulus

Young's modulus is derived from Hooke's Law which is a principle of physics that states that the force needed to extend or compress a spring by some distance is proportional to that distance [17]. Atomic structures behavior under stress and strain is modeled in a similar way. Young's modulus describes the material's strain response to uni-axial stress in the direction of this stress. It's a measure of a materials ability to withstand changes in length when under lengthwise tension or

compression. Young's modulus measures elasticity and can be referred to as the elastic modulus [18]. This material property is calculated by dividing the stress by the strain. Stress is the force divided by surface area and strain is the change in length divided by the original length in the direction of the force [19].

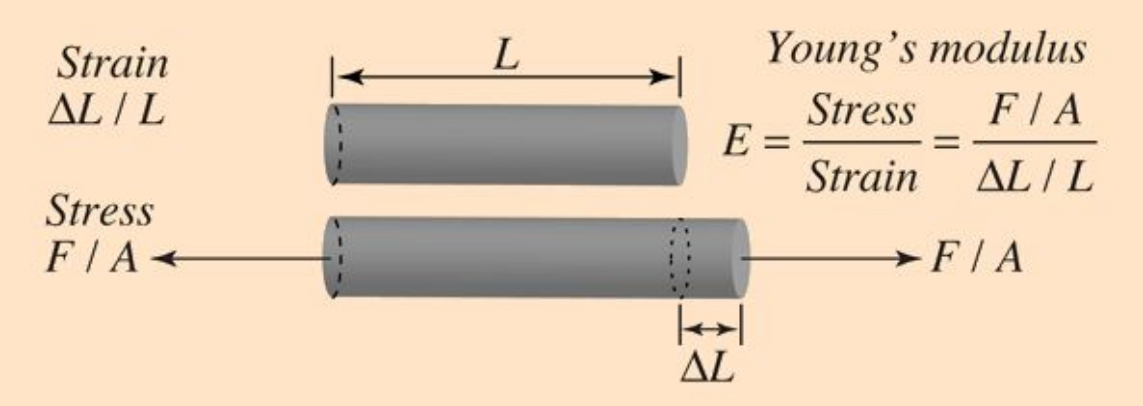

Figure 1.4: Illustration of Young's Modulus and how to calculate it [19]

This means that when the inter-atomic spacing is larger than it's unstressed value, the attractive forces between the atoms must be greater than the repulsive forces since the attractive forces balance both the repulsive forces and the external forces of tension or compression. Conversely, the repulsive forces between the atoms must be greater than the attractive forces when the inter-atomic spacing is less than its unstressed value. Young's modulus of the silica material used in the suspension system is utilized in the calculations of different types of noise which are essentially tracking the ways the material is losing energy and creating a noise that is interfering with the detection of the gravitational waves in the ground based interferometers.

1.7 Production of Silica Fibers

A fiber pulling machine was designed in order to pull the silica fibers to a precise diameter. The fiber pulling machine uses a high acceleration pulling stage in combination with a CO_2 laser focused onto the silica stock fiber head which heats it and allows for a controlled pull and fiber profile [20].

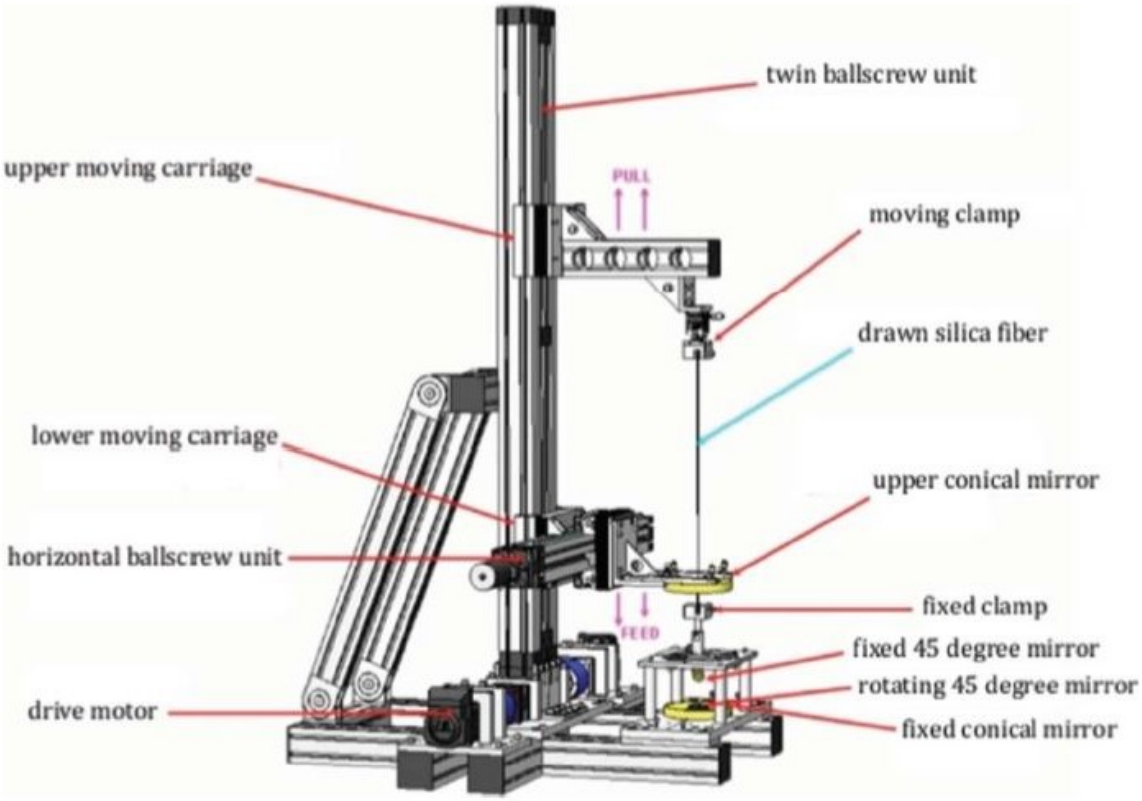

Figure 1.5: CAD Drawing of the aLIGO pulling machine with all major components labeled [4, 12].

In 2015 a thin fiber pulling machine was developed in order to pull fibers with a diameter less then $20\mu m$ [4].

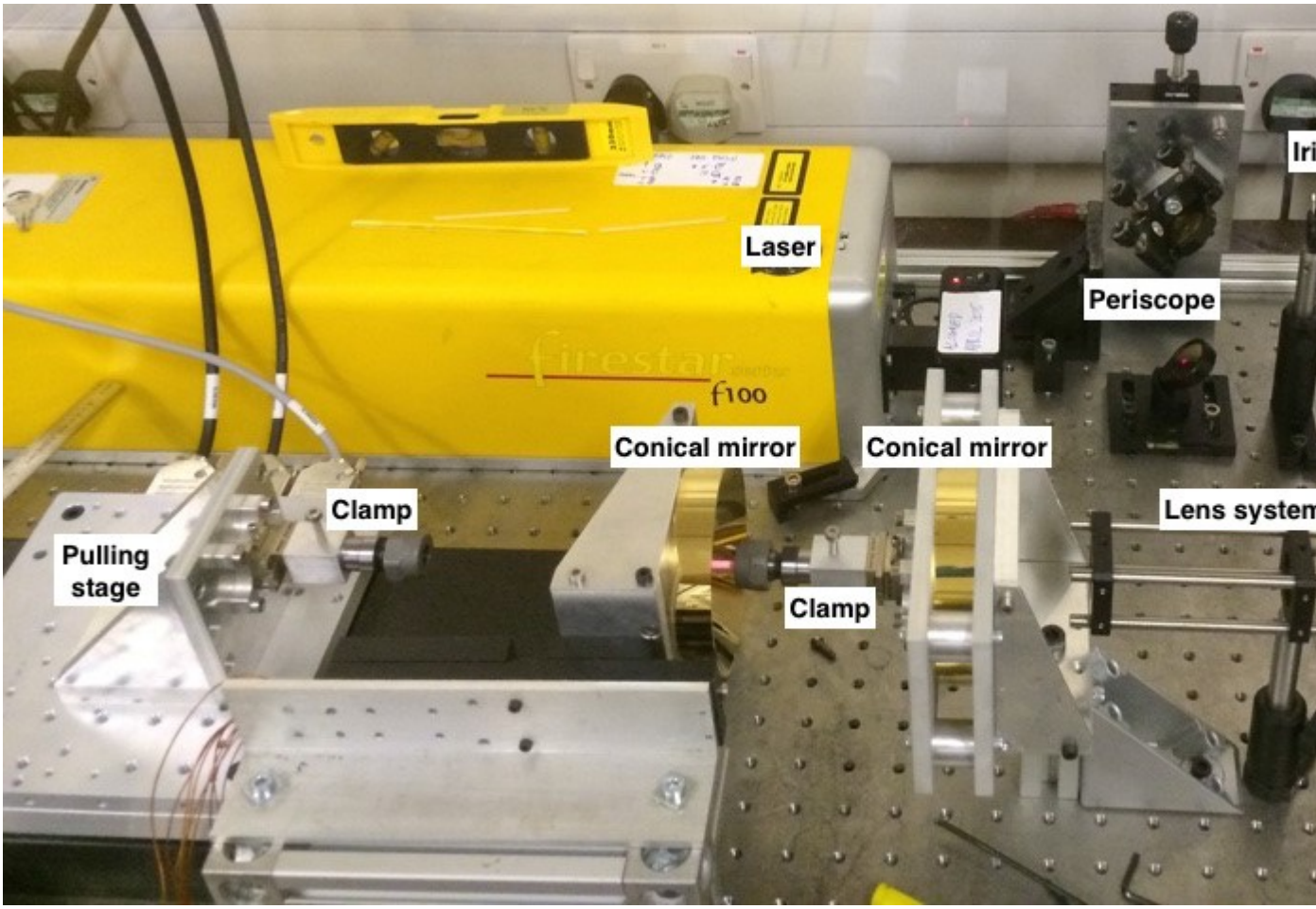

Figure 1.6: Image of the thin fiber pulling set up that shows the lazor configuration, lens system, conical mirrors and the pulling stage [4].

1.8 Silica Fibers

The fused silica fibers have many advantages over the previous steel wire material. Fused silica has a tensile strength well above steel and level of internal friction is much lower than steel [10]. Another benefit to this material is that research revealed that the silica fibers geometric shape could produce a force that would result in a reduction of noise from thermoelastic loss [10, 21].

1.9 Previous Strength Testers

The first strength testing machines developed at IGR for the silica fibers was in 2002 by Alastair Heptonstall and other [22]. In 2008 the IGR MKII was the next iteration of the strength testing machine developed. Some of the design goals of the IGR MKII was to include the ability to do

vertical or horizontal tests, increase load capacity, maintain adjustability for sample lengths, fine control over speed loading and be able to introduce rotation during loading [22].

In 2013 Gregor Taylor wrote his honors project report on the design of the next iteration of strength testers, the MKIII IGR Strength testing unit [21]. This strength testing machine is smaller and fits on a table top and allows for small fiber tests. This is the strength tester that I worked on upgrading. Figure 1.7 is a diagram of the initial design of the MKIII and with its components labeled.

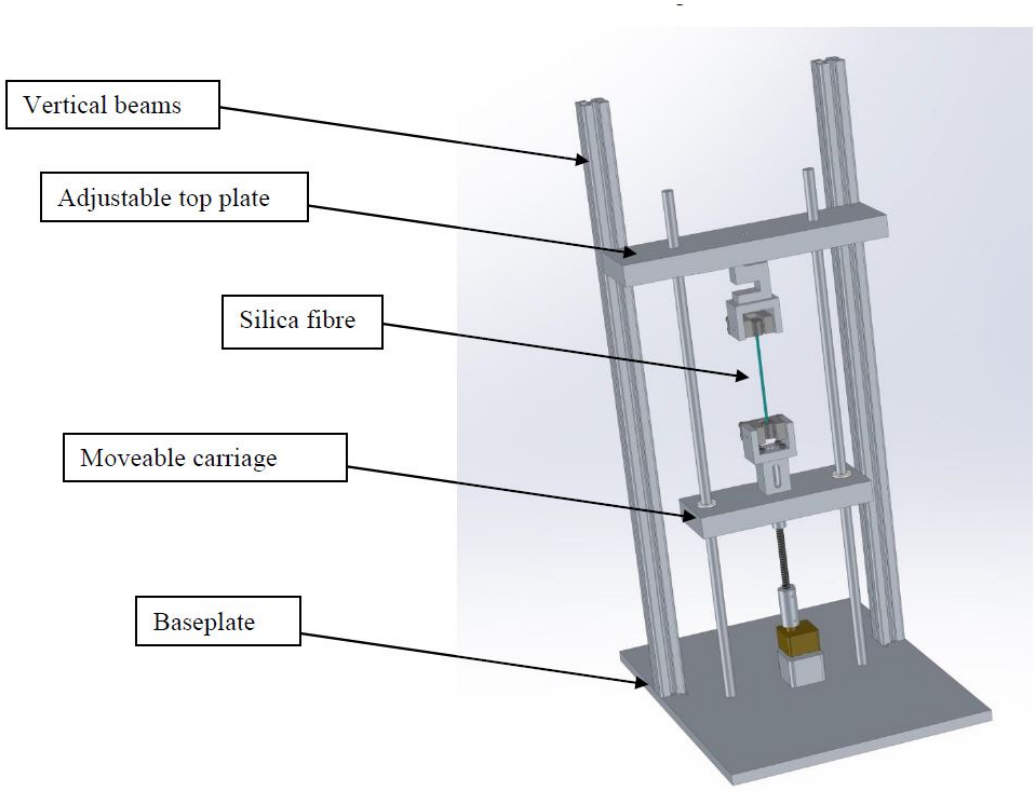

Figure 1.7: Initial Design of the MKIII IGR [21].

The drive assembly includes an Astrosyn Y-129 stepper motor paired with a 100:1 gearbox to allow for accurate pulling of the fiber [21]. It's connected to a RSSM2 Stepper Motor drive board which is linked to an Arduino Duemilanove micro-controller that connects to LabVIEW. A 12 V power supply is connected to the RSSM2 to power the motor. The drive assembly was attached to a precision ball screw that goes through an aluminum bridge piece to attach to the moving platform and fiber anchoring system. The design allowed for the motor to rotate which rotated the ball screw and exerts a downward force on the nut and in turn on the fiber. The maximum force that the motor and gearbox could exert was calculated to be 95000 N if the stepper motor was operating at its maximum torque of .09 Nm [21]. In order to increase the stability of the moving platform,

it has two vertical guide poles through the platform on either side of the fiber anchoring system to act as vertical bearings. At the top of the strength tester, the other end of the fiber anchoring system attaches to an Omega S-Beam DP25b load cell which records loads up to 11.3 kg [21]. The end piece is a 13 mm by 17 mm box that has a black plastic spacer for an aluminum end piece as seen in figure 1.7.

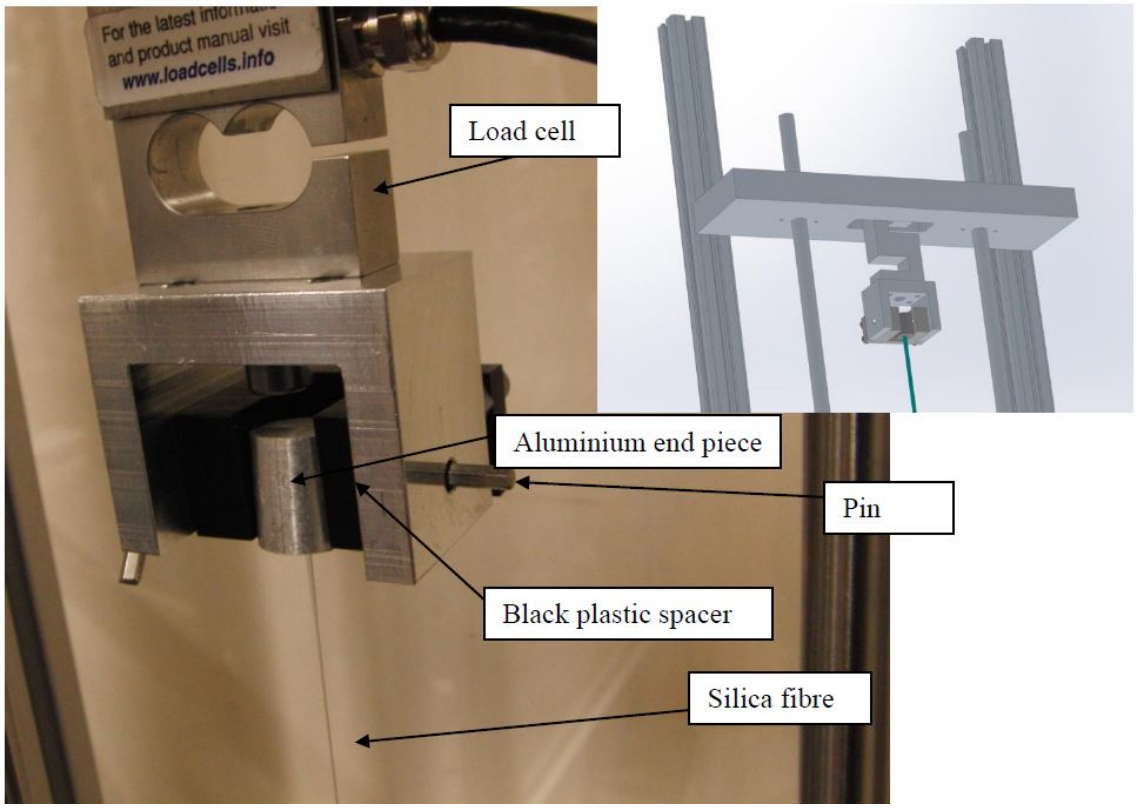

Figure 1.8: Anchor Assembly with parts labeled. [21]

2 Updating the Strength Tester

Updating the strength tester is an ongoing project. The improvements made during this summer internship are described below.

2.1 Mechanical Improvements

One of the goals of updating the small strength tester was to improve the mechanical design. The gearbox had a slight rotation due to the screws not holding it stationary to the base. This resulted in a small error that came from the motor steps being inconsistent between runs as it used some of the steps to rotate the loose gear box. Another update included mounting two micro-controllers at the

top and two at the bottom of the limits of the stage in order to have a stopping mechanism. Some of the wiring for the Arduino was upgraded as well. The previously written LabVIEW program was updated in order to incorporate the magnetic encoders counts and convert it to displacement within LabVIEW. The load cell was connected through LabVIEW as well. The majority of this project was spent on installing a linear magnetic encoder and the magnetic strip, which will be described below.

2.1.1 Stabilize Gear Box

The gear box was previously affixed to the base of the strength tester with two screws. It had a tenancy to twist when it first started rotating. To increase the stability, two more screws were added in along with 4 plastic supports to secure them as seen in figure 2.1.

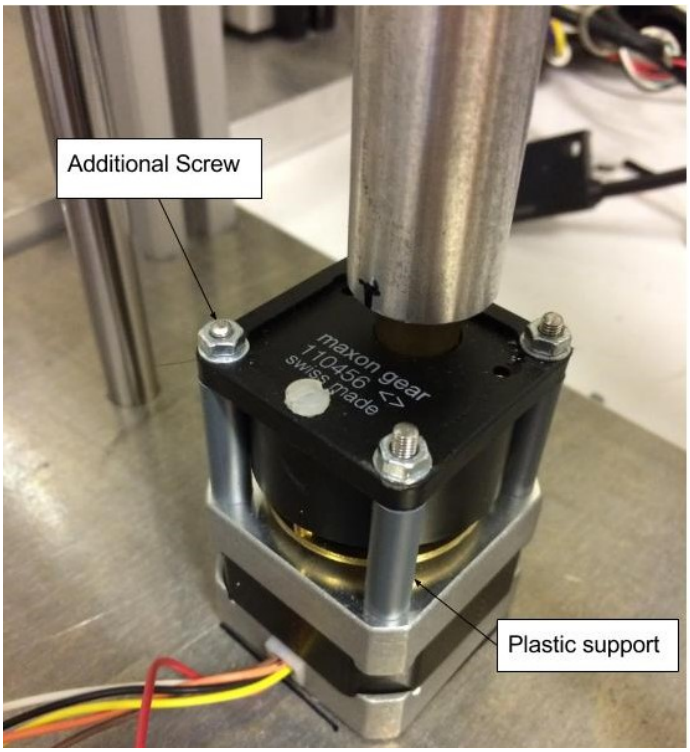

Figure 2.1: Added in additional screws and plastic supports to gear box attachment.

2.1.2 Installation of magnetic encoder mount

The linear magnetic encoder and the magnetic strip were mounted onto the small strength tester by adding in a 3rd Bosch bar slightly off center to the back of the stage. This was to hold the magnetic strip close to the encoder which was mounted at the back middle of the stage. This location was chosen in order to reduce any error that might result from taking a measurements off of the the side of the stage, which can wobble more then the middle.

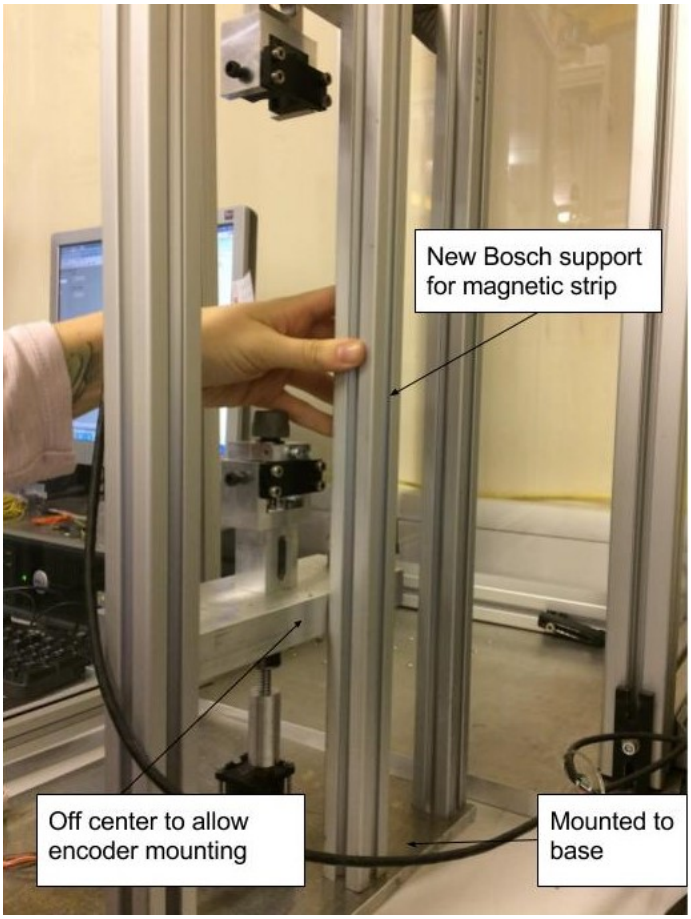

Figure 2.2: Image showing where the third Bosch bar was planned to be installed.

2.2 Linear Magnetic Encoder

The linear magnetic encoder used for this project is the SIKO MSK5000-0373 linear magnetic encoder along with the MB500/1 incrementally coded magnetic band. The MSK5000-0373 encoder is an incremental digital interface encoder with a resolution of 1 μm [23]. Once the mechanical components for the installation of the linear magnetic encoder were in place, a small electronics box was made in order to connect the encoder to a National Instruments 6008 USB DAQ Board [24] and test before installation. This was made to connect the A channel, B channel, power and ground to appropriate connections using banana clips which allowed for portability and testing as seen in figure 2.3.

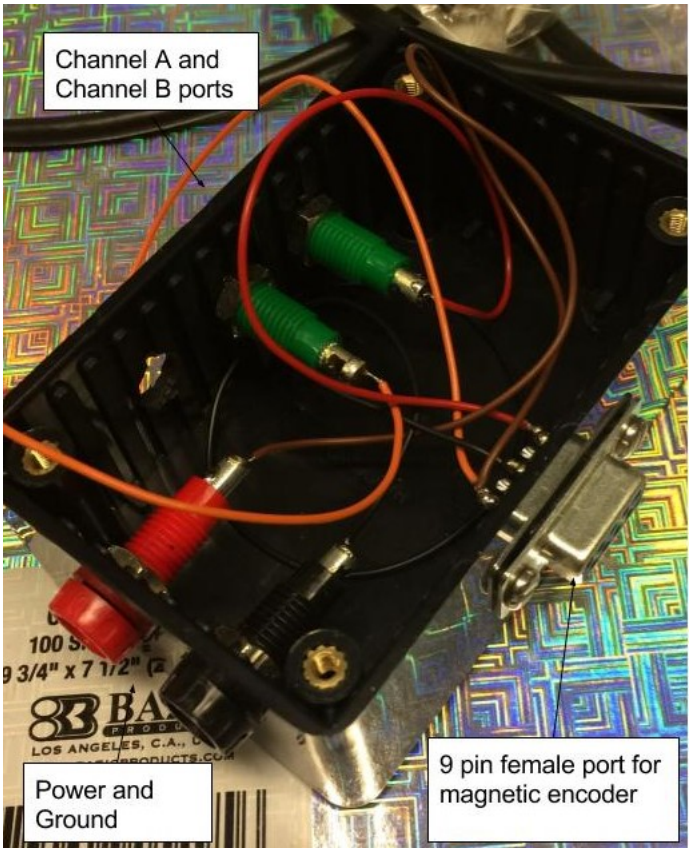

Figure 2.3: Linear Magnetic Encoder connector for National Instruments 6008 Counter.

We tested the MSK5000-0373 encoder and magnetic strip with a simple LabVIEW National Instruments test program in the Labview Device Management software. The program counted the pulses produces by the magnetic strip but as we ran the program for a specific distance and we saw a huge difference in the counts that it measured.

Test Run	Start Caliper (mm)	End Caliper (mm)	Caliper Displacement (mm)	Magnetic Encoder Count	mm/M.E. Count	M.E. Count/MM
1	73.3	73.6	0.30	2485	1.21E-04	8283.333
2	73.6	72.4	1.20	197342	6.08E-06	164451.667
3	72.4	71.4	1.00	139225	7.18E-06	139225.000
4	71.4	70.1	1.30	120284	1.08E-05	92526.154
5	70.1	69.1	1.00	122203	8.18E-06	122203.000
6	69.1	68.6	0.50	128155	3.90E-06	256310.000

Figure 2.4: Table of initial test measurements of MSK5000-0373 linear magnetic encoder.

2.2.1 Trouble Shooting

The first step in understanding where the issue was in the MSK5000-0373 linear encoder was to connect the encoder to an oscilloscope. We set up a test environment where the MB500/1 magnetic strip was attached to a micrometer and the MSK5000-0373 linear encoder was clamped stable. This allowed us to move the encoder along the magnetic strip at a controlled pace and measure the distance while observing the oscilloscope. The MSK5000-0373 encoder produced a square wave with bounce on both the falling and the rising edge. An example of what bounce on the falling edge looks like is shown in figure 2.5.

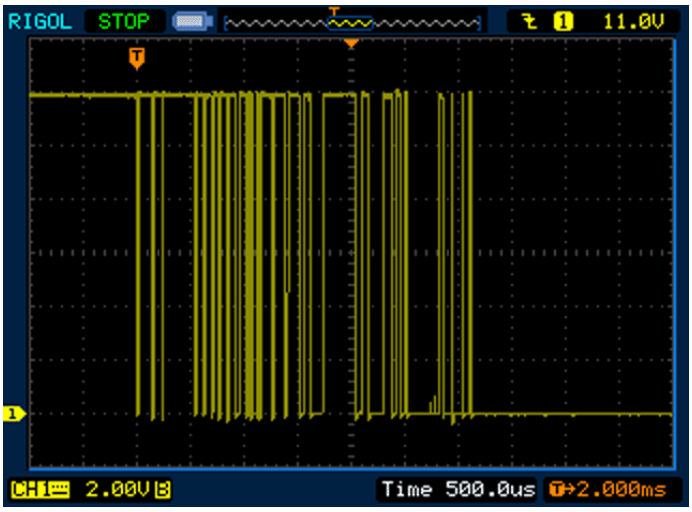

Figure 2.5: Example of bounce produced on the falling edge of a square wave on a relay contact bounce [25].

When we connected the MSK5000-0373 encoder to the National Instruments 6008 USB DAQ Board and the oscilloscope, we confirmed that the NI 6008 USB DAQ Board count would rapidly increase while the MSK5000-0373 encoder was at either the falling or rising edge where the bounce was occurring.

Once we realized that the MSK5000-0373 encoder had bounce we tried a number of ways to fix it. We knew that the large laser fiber growing system had the same model MSK5000-0373 encoder to measure linear displacement as well as the two fiber profiling machines in the lab which had different models: MSK320-0012 linear encoder and LabJack U12 counter. We tried many different test scenarios in order to understand why MSK5000-0373 encoder with the National Instruments 6008 USB DAQ Board combination wouldn't produce a reliable measurement of the distance traveled by the stage. We changed out the counter from the NI 6008 USB DAQ Board to the NI 6211 USB DAQ Board which still produced the bounce and inaccurate count. Research was done on how to create an integrated circuit in order to cancel out the bounce. A circuit was made for one of the other linear encoders on a small fiber profile which used MSK320-0012 linear encoder and LabJack U12 counter. We connected that circuit to the MSK5000-0373 encoder and it still produced a bounce.

It wasn't until many different combinations of parts that we realized what the issue was.

Test Case	Blue Encoder	Black Encoder	6008	6211	Labjack	MB500/1 tape	MB500/1 tape WITH COVER	Tape on large laser	Circuit from profiler	Laptop	Desk Top	Counter/Comp from large laser	Bounce	No Bounce
1	■		■			■				■			■	
2	■		■			■					■		■	
3	■		■			■			■	■				
4	■		■			■			■		■		■	
5	■			■		■				■			■	
6	■			■		■					■		■	
7	■			■		■			■	■			■	
8	■			■		■			■		■		■	
9	■					■						■		■
10		■	■			■				■				
11		■	■			■					■		■	
12		■	■			■			■	■				
13		■	■			■			■		■			
14		■		■		■				■			■	
15		■		■		■					■		■	
16		■		■		■			■	■				
17		■		■		■			■		■			
18		■				■						■		■
19		■		■				■			■		■	
20		■			■			■			■		■	

Figure 2.6: Table of test scenarios where the shaded boxes are the components included in the test and the last two columns show if bounce was produced on the falling and rising edge of the square wave. Blue encoder is the MSK5000-0373 used from the start of the experiment and the black encoder is the MSK5000-0373 taken off of the large laser fiber growing system.

After many different iterations and test scenarios, we narrowed it down to two cases in which the MSK5000-0373 encoder worked with out bounce. Both of those test scenarios used the PCI card in the large laser fiber growing system to count the bounce. We tested the MSK5000-0373 encoder with the same model of PCI card on a different computer and it produced a reliable square wave with no bounce. The MSK5000-0373 encoder only worked was with the PCI card as a counter for its two channel square wave. The two channels meant that it is able to only count a pulse when it had one channel falling or rising while the other is not which results in not counting the bounce. The figure 2.7 shows how a two channel square wave produces counts in the X1, X2 and X4.

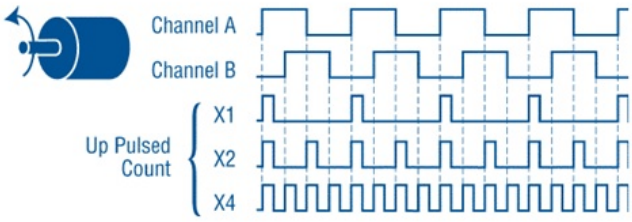

Figure 2.7: X1, X2, and X4 refers to the amount of counts it can take across a distance. Image shows three different count types [26].

The MSK5000-0373 encoder has two channels and are able to have a more accurate reading on a measurement of distance while the MSK320-0012 linear encoder used in the profiling machines did not have this capability. They are designed for less precision which results in a larger square wave.

2.3 Arduino

The updates to the Arduino Duemilanove were minor and including updating the wires so they had connectors that fit more securely into the Arduino. We also wiped the code of the Arduino, did a test run with a blinking light code to make sure the Arduino was working properly. We then re-installed the LabVIEW code that required to be on the Arduino in order for LabVIEW to communicate with it. The code is provided by National Instruments and called LIFA_BASE.ino. It is best to upload the code to the Arduino and close out the Arduino interface as per the recommendation of LabVIEW's forums. Through our testing, we discovered that when LabVIEW is communicating with Arduino if you shut off the code, this can cause the next run of the LabVIEW program through Arduino to cause an error message. If you run a LabVIEW program through Arduino when the LabVIEW system stop button is used instead of the programming coming to its logical stop, Arduino will produce an error message for that run and the next run, the program will work again. We think this is because the Arduino board is unable to stop the code midway through execution and sends an error message to LabVIEW.

2.4 LabVIEW

The original program written for the MKIII small strength tester was called "Stepper_2". It had the ability to run the Arduino which controlled the stepper motor. The block diagram is shown in Appendix B.

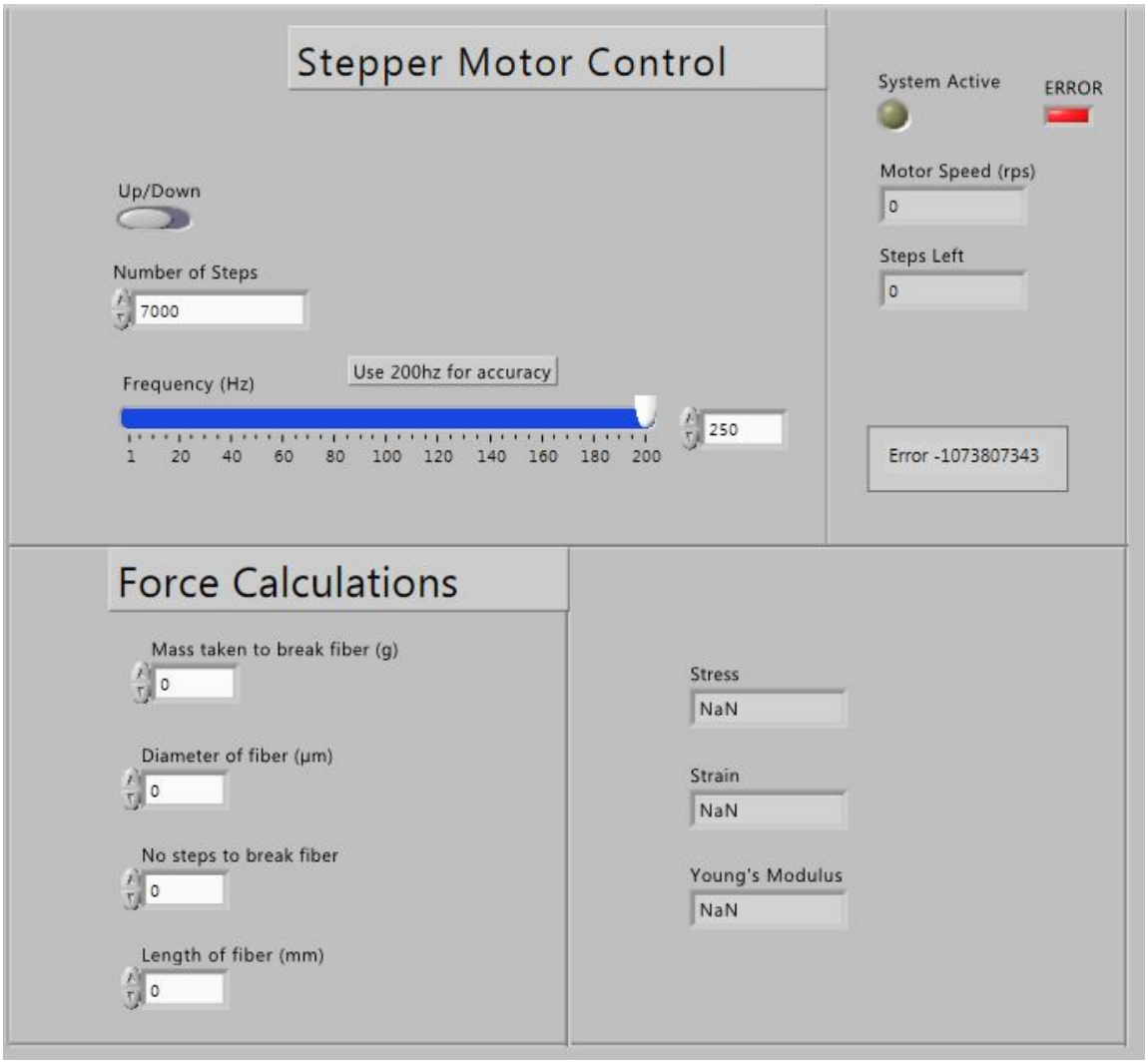

Figure 2.8: The original Stepper_2 Program for the MKIII Small strength tester.

The updated version of the program is called Stepper3_V5 and has the ability to run the Arduino and motor, as well as the load cell and linear encoder through the PCI in the large laser crystal growth computer. The program was written so that the Arduino would move the motor an increment of steps, wait a period of time, take measurements from the load cell and linear encoder and then repeat the Arduino/motor action and measurements until the number of iterations is completed.

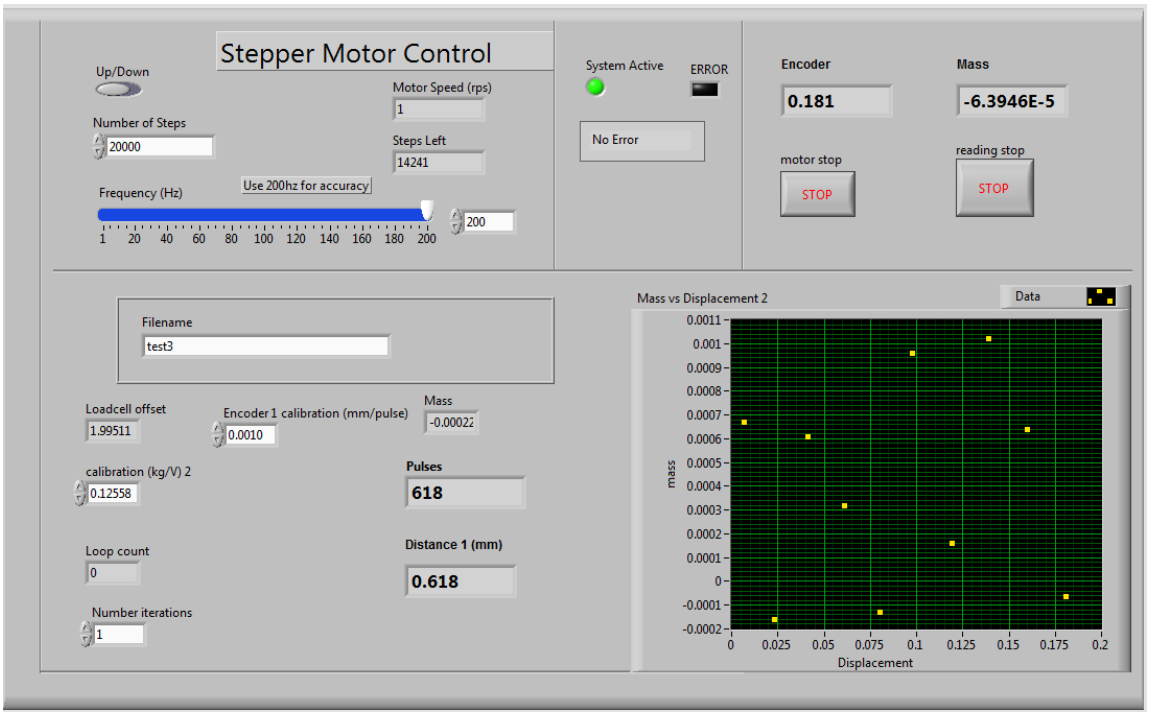

Figure 2.9: Updated LabVIEW front panel for the Stepper3_V5 program.

2.5 Micro-Controller Switches

In order to have a LabVIEW based code stop and a final mechanical stop, two micro-controllers were installed in parallel on the outer Bosch frame. The legs of the micro switched were bent in order to have the right spacing to shut the switch when making contact with the stage. The wires were made longer in order to connect to the Arduino and with connectors that make disconnecting from the micro-controllers easier. At the top, the outer most micro-controller was intended to be a kill switch that would connect to a manual reset button. The inner micro-controller was intended to be connected to the Arduino in order to be a code off switch. The reverse set up is at the bottom with two micro-controllers, the outer being the total shut off and the inner being the code shut off. They were installed but have yet to be incorporated into the LabVIEW and Arduino code, or connected to the manual switches.

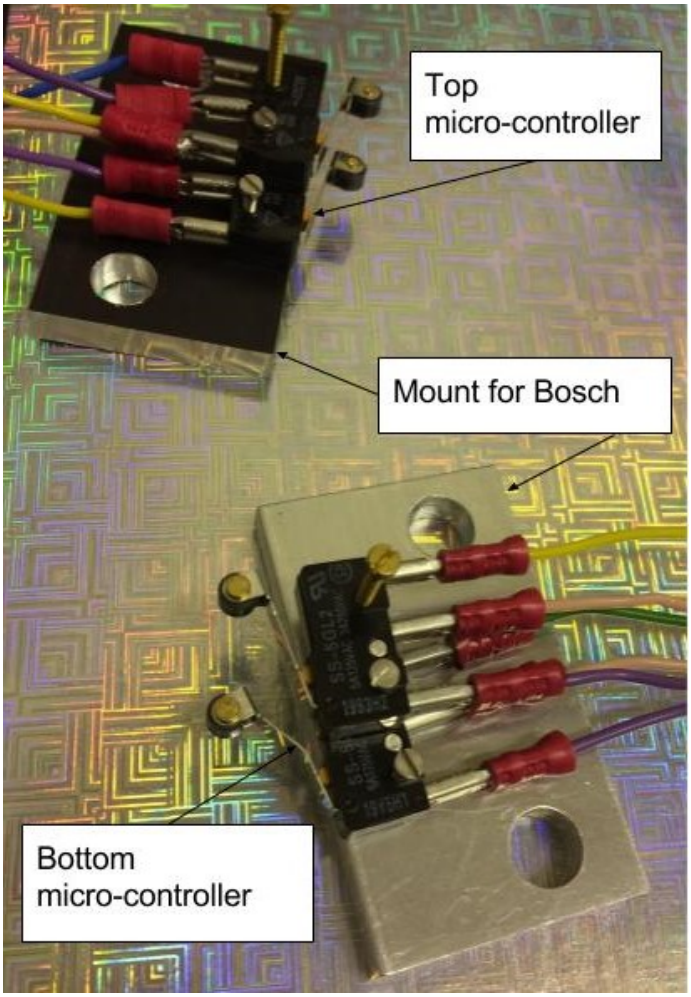

Figure 2.10: Image of the top and bottom micro-controller switches to disengage strength tester.

2.6 Real Time Load Calculations

The Omega S-Beam DP25b load cell was connected to the NI 6008 USB DAQ Board which was plugged into LabVIEW through USB. A simple voltage counter reading program was used in LabVIEW to take in the voltage readings which are converted to kg. The offset is programmed into LabVIEW and the conversion from voltage to kg has to be entered into the LabVIEW front panel.

2.7 Analysis

A large portion of the time spent on this project was on figuring out how to combat the bounce of the falling and rising square wave from the linear encoder. A greater understanding of which counters and encoder combination worked to track displacement was gained and will be helpful to

future projects that require the use of a linear encoder, especially when a high amount of precision is needed, to the order 1 μm resolution [23]. More updates would be useful to improve the usability of the strength tester and are discussed below.

3 Strength Testing

The MKIII Strength Tester was assembled with the MSK5000-0373 encoder connected to the large laser PCI computer, an updated Arduino Duemilanove, load cell connected to NI 6008 USB DAQ Board which were all powered and ran through LabVIEW.

3.1 Calibration

In order to check what the conversion between the MSK5000-0373 encoder count and distance traveled as well as the stepper motor steps and distance traveled, an initial calibration was done. The motor was moved 10,000 steps in one direction and the distance traveled by the stage was recorded from digital calipers. The count from the encoder was also recorded every 10,000 steps as well as the displacement. In figure 3.1 you can see that the average mm/count is a .001 conversion factor and the average mm/step is a .0001 conversion factor. This supports the resolution listed for the linear encoder as .001 mm [23].

Round	Up/down	Start time	End Time	Steps	Start Caliper (mm)	End Caliper (mm)	distance traveled (mm)	Total count at the end of the run	Count per run	mm/count	mm/steps
6	up	12:03	12:10	10000	55.99	57.34	1.35	1103	1103	0.001224	0.0001350
7	up	12:11	12:19	20000	55.99	58.26	2.27	2198	1095	0.001033	0.0001135
8	up	12:20	12:27	30000	55.99	59.3	3.31	3311	1113	0.001000	0.0001103
9	up	13:01	13:10	40000	55.99	60.58	4.59	4424	1113	0.001038	0.0001148
10	up	13:11	13:20	50000	55.99	61.83	5.84	5518	1094	0.001058	0.0001168
Round	Up/down	Start time	End Time	Steps	Start Caliper (mm)	End Caliper (mm)	distance traveled (mm)	Total count at the end of the run	Count per run	mm/count	mm/steps
11	Down	13:20	13:29	10000	61.83	60.61	1.22	1017	1017	0.00120	0.000122
12	Down	13:29	13:37	20000	61.83	59.34	2.49	2114	1097	0.00118	0.0001245
13	Down	13:38	13:46	30000	61.83	58.36	3.47	3221	1107	0.00108	0.000115666666
14	Down	13:48	13:55	40000	61.83	57.11	4.72	4337	1116	0.00109	0.000118
15	Down	14:06	4:17	50000	61.83	55.06	6.77	5426	1089	0.00125	0.0001354
16	Down	14:18	14:24	60000	61.83	53.92	7.91	6538	1112	0.00121	0.000131833333

Figure 3.1: Data taken in order to calibrate the displacement of the stage per steps of the motor and displacement of the stage per linear magnetic count.

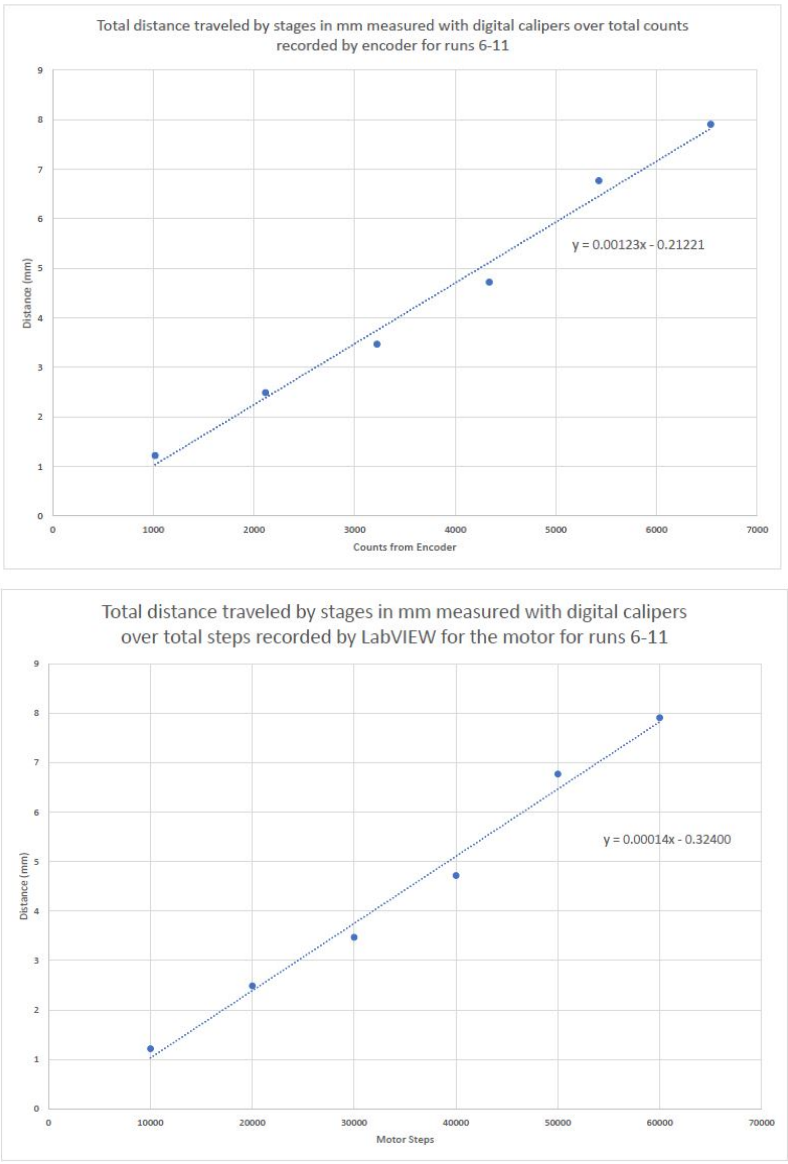

Figure 3.2: Top graph is showing distance traveled by the stage in mm measured with calipers per every 10,000 steps, vs the counts recorded by the linear encoder per every 10,000 steps. The trend line shows the slope of .001 which is the mm/count conversation factor. Bottom graph is showing distance traveled by the stage in mm measured with calipers per every 10,000 steps, vs the steps in 10,000 steps increments. The trend line shows the slope of .0001 which is the mm/steps conversation factor.

The load cell should also be calibrated regularly to make sure the voltage to kg conversion is

correct. LabVIEW device management software allows for testing of the load cell. By placing a known kg mass on the load cell and recording the voltage from it, a conversion of kg per volts is made. Also comparing the voltage reported with no mass and with a known mass will tell you what the offset of the load cell reading is which is programmed into the LabVIEW code to automatically update.

3.2 Fiber Profiles

A batch of fibers was pulled with the small fiber puller mentioned previously in order to test on the updated strength tester. The diameter information was taken through with the small fiber profiler. We performed the strength test on three fibers and were able to save the data on two of them. One of the tests crashed in Labview and didn't save the load or displacement data.

3.3 Strength Testing Methods

The MKIII Strength testing machine procedures were outlined as follows:

1. Calibrate the load cell as described above. Input the calibration into LabVIEW.
2. Move the stage to the correct location. Load into the top and bottom clamps, load in the fiber cartridge into the top and bottom black plastic holders and secure with screws. The black plastic holders are labeled with B for bottom and T for top. Make sure to remove the vertical metal stays on the cartridge.
3. LabVIEW set up:
    - Set number of steps to 200, this is the steps the motor takes
    - Set Frequency to 200
    - Type in name of the file in. This will save the file in the Data (D:)/strengthtester folder in a folder label with the date of the test.
    - Set encoder calibration to .0010 mm/pulse, this is based off on the calibrations done earlier
    - Set number of iterations to 200, this is the number of times it goes through the number of steps set earlier
    - Select "down" from up/down toggle
4. Press start button at top of LabVIEW. Press reading stop button at the right of the front panel to stop LabVIEW code with out crashing Arduino.
    - Note: Avoid stopping the program before the Arduino code (iterations of the motor steps) have been completed. This might result in the LabVIEW program not running again. If this happens, run it again with out using the hard stop through Labview. Let the program complete before using the stop button at the right of the screen for the load cell measurements and linear encoder measurements. The Arduino code will only run after the logic of the LabVIEW code has been completed, not if it has been stopped with the hard stop button at the top of the screen.

3.4 Strength Testing Results

The two fibers that we were able to collect data were run 200 steps, 200 times and we collected 200 data points. The data points of displacements vs load was used along with the fiber profile to calculate the stress and strain in order to plot Young's modulus. Below is the breaking force and breaking stress for the two fibers. Breaking force is calculated with the force measured with the load cell at the time the fiber broke and including a ±.25 % error for the load cell measurement [21].

The calculation for the breaking stress error is calculated:

$$\frac{\delta\sigma_{breaking}}{\sigma_{breaking}} = \sqrt{\left(\frac{\delta F}{F}\right)^2 + \left(\frac{\delta A_{min}}{A_{min}}\right)^2} \tag{3.1}$$

Where $\sigma_{breaking}$ is the breaking stress, F is the force measured by the load cell, δF is the error in the load cell which is ±.25% [21] , A_{min} is the minimum area of the fiber taken from the fiber profiler and δA_{min} is the error in the area which is ±12%. It was calculated with the error of diameter of the wire used to calibrate the fiber profiler [4]. The error in the length of the fiber was calculated during the fiber profiling process and was given as ±.002% error from the pulling stage data sheet [27].

Fiber Number	**Breaking Force (N)** ±.25%	σ **Breaking Stress (GPa)** ±5%
1	.044 ±.00001	3.012 ± .151
2	.137 ± .0003	2.637 ± .132

Table 1: Breaking Force and Stress

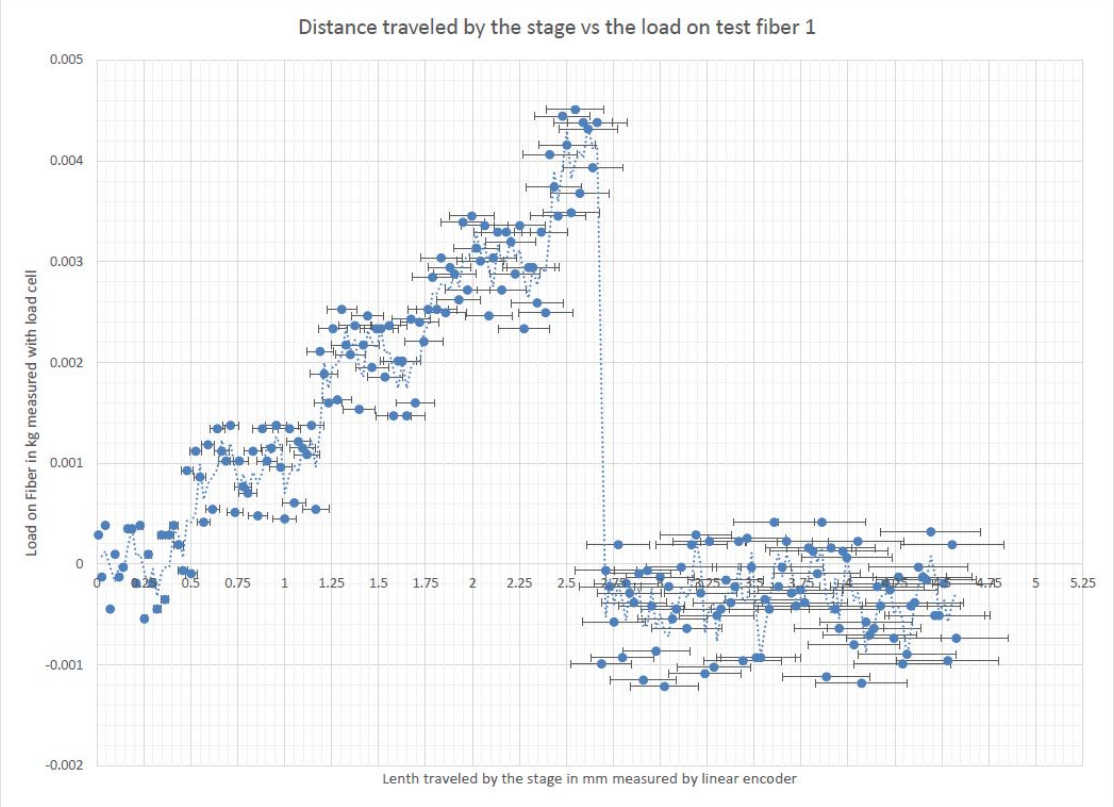

Figure 3.3: Graph of the distance traveled by the stage in mm measured by the linear encoder with a error of $\pm 6\%$ vs the load applied to the fiber measured by the load cell with a error of $\pm .25\%$ for fiber 1. The data points at the end are after the fiber broke.

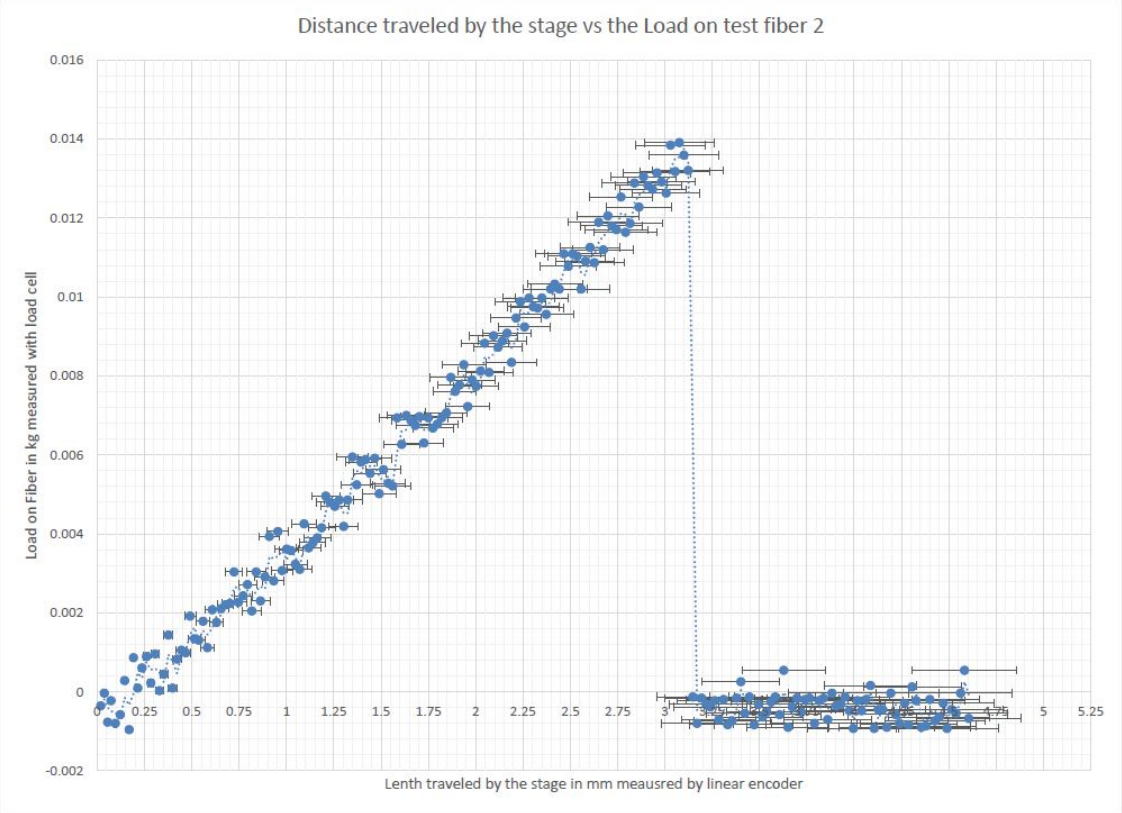

Figure 3.4: Graph of the distance traveled by the stage vs the load applied to the fiber for fiber 2. The data points at the end are after the fiber has broke.

3.4.1 Young's Modulus

Young's modulus assumes that there is a uniform radius across the thin length of the fiber. The fiber profile shows that the radius is not uniform and can deviate away from the average by as much as 15 μm [21]. For the calculation of Young's modulus, the smallest diameter from the fiber profiling was used. Young's modulus is defined as:

$$Y = \frac{Stress}{Strain} \tag{3.2}$$

Where stress and strain are defined as:

$$\sigma = \frac{F}{A} \tag{3.3}$$

$$\epsilon = \frac{\Delta L}{L} \tag{3.4}$$

The symbol for stress is σ, F is the force applied on the fiber, and A is the cross section area of the fiber. The symbolϵ is the stress, ΔL is the change in length, and L is the original length. The error for the length of the fiber is based on the error of the pull stage which is $\pm.002\%$ [27]. The error in the change of length is based on the encoder and is $\pm 6\%$ [23].

The error for the strain of the fiber is defined as:

$$\frac{\delta\epsilon}{\epsilon} = \sqrt{\left(\frac{\delta\Delta L}{\Delta L}\right)^2 + \left(\frac{\delta L}{L}\right)^2} \tag{3.5}$$

The same formulation is used for the error in stress, where instead of the change in length and length, the force and area are used. The error for Young's modulus is calculated using this equation:

$$\frac{\delta Y}{Y} = \sqrt{\left(\frac{\delta\sigma}{\sigma}\right)^2 + \left(\frac{\delta\epsilon}{\epsilon}\right)^2} \tag{3.6}$$

	Fiber 1	**Fiber 2**
Stress Error	$\pm 5\%$	$\pm 5\%$
Strain Error	$\pm 24\%$	$\pm 24\%$
Young's Modulus (GPa)	28 ± 6.72	84 ± 20.16

Table 2: Young's modulus results

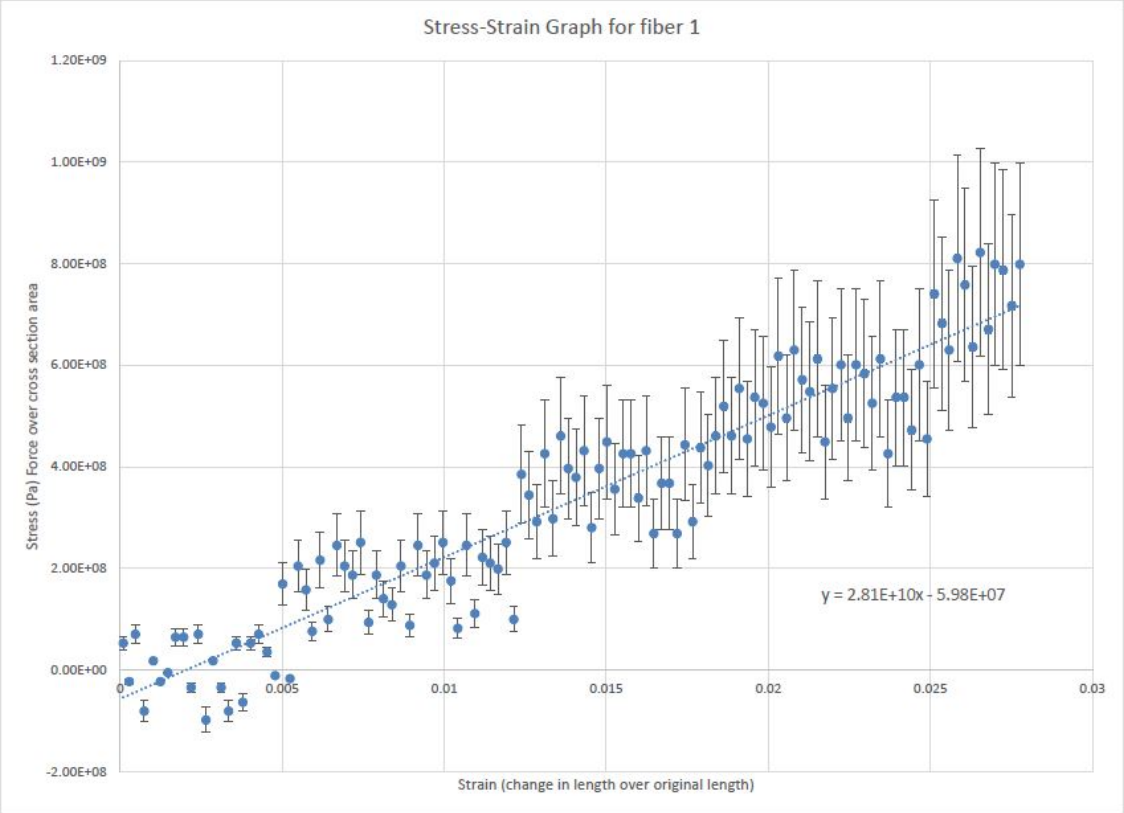

Figure 3.5: Graph of Young's modulus for fiber 1.

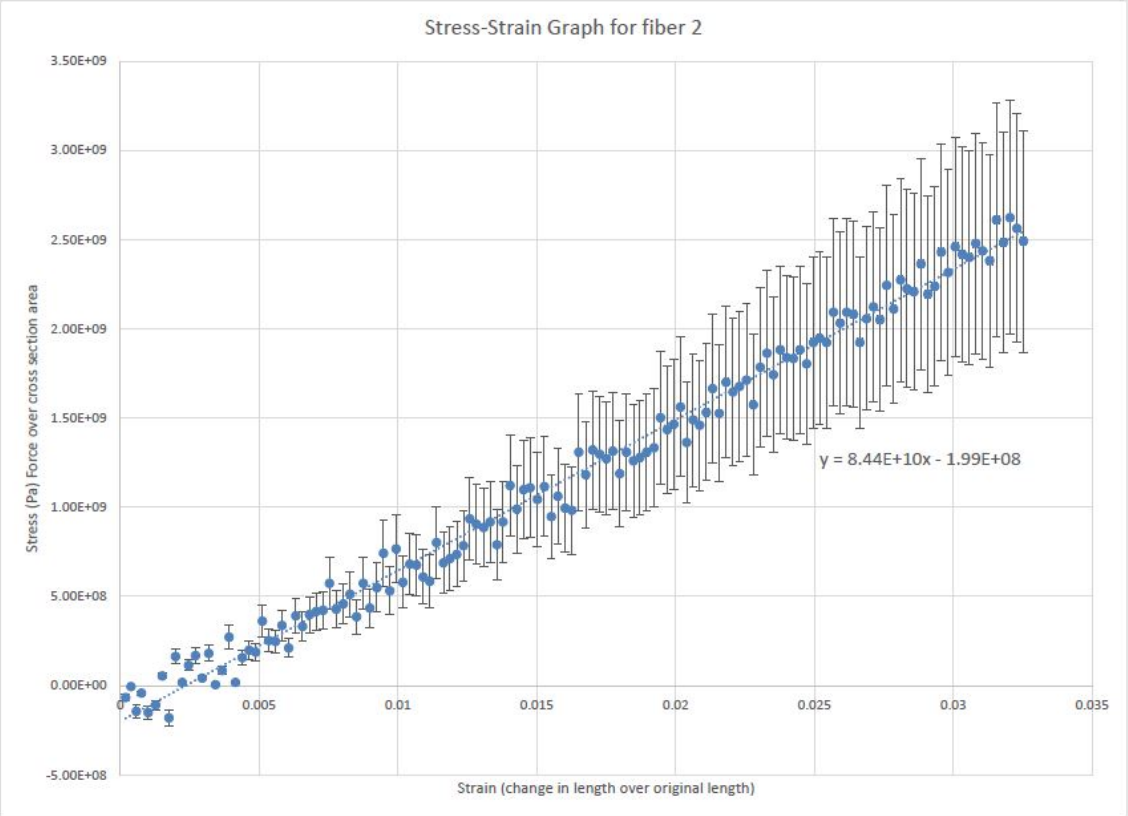

Figure 3.6: Graph of Young's modulus for fiber 2.

3.5 Analysis

The accepted value for Young's modulus of bulk fused silica is 73 GPa [28]. Theoretically, once the diameter of the fiber goes below a certain thickness, Young's modulus will increase as it changes from bulk characteristics to surface characteristics [4]. Both of the fibers tested had different values of Young's modulus calculations. If there were any surface cracks in the fibers, that would weaken it and produce a low Young's modulus like with fiber 1. Fiber 1 broke in less distance then the second fiber did and the second fiber test results were closer to the other test results on similar fibers. Fiber 2 is closer to other experimental results than fiber 1. The error is large which could put it closer to the accepted value. More testing will need to be done in order to get enough data to analyze the material properties further.

4 Future Work on MKIII Strength Tester

There is a lot of ways that the MKIII Strength Tester could be improved upon in order to make it more user-friendly, reduce error, and maximize its strength testing capabilities. Many of the

improvements are listed in Gregor Taylor's project report [21].Through working with the strength tester other improvements were made clear.

4.1 Increase height of tester

The height of the two round support beams is the current limitation on the length of the fibers that the strength tester can test. The machine is set up to test smaller fibers but increasing the guide polls would allow for a wider range of the small fiber lengths. It would also allow for more room to have to test materials that might stretch longer than the fibers.

4.2 Micro-encoders

The micro-encoders were not installed because of time limitations. Installing both sets of them will give the strength tester appropriate stopping capabilities in case the stage accidentally goes past where it can go with out harming the other components of the strength tester. Two of the encoder needs to be wired to manual stop buttons and two of them need to be wired into the Arduino to act as code stop if the switch is compressed.

4.3 Arduino

The box that the Arduino and motor controller in is too small to house the wires in a way that doesn't push them out. Reconstructing the casing along with reinforcing the wiring would reduce the risk that the wiring comes loose. Where the box is in relation to the encasement of the strength tester could be engineered in a way that was more user-friendly. Right now the door on the cage doesn't close because of the wiring from the Arduino, motor and load cell. The wiring from the motor to the motor control board is too short to be able to pull the Arduino out of the clear cage that houses the strength tester.

4.4 LabVIEW

The framework in LabVIEW runs but not in the most efficient way. Currently, you have to manually set the iterations, which is the number of rounds that it runs the set amount of steps that you enter into the program. Ideally, the program would check every 200 steps if the load cell was at zero and this would indicate that the stage doesn't need to keep moving down. The logic to improve the program can be worked out and implemented.

5 Conclusion

The MKIII is still in the process of being updated. The majority of the 10 weeks was spent on researching, troubleshooting and connecting the MSK5000-0373 linear encoder. Signal bounce is a common issue in electronics and understanding how the magnetic encoders work was crucial to being able to use them. More improvements can be made to the strength tester and additional tests on different fibers would be useful to understand Young's modulus, specifically for geometries where the surface area is in a much larger ratio to the internal area such as with the thin silica fibers.

6 Acknowledgments

I am grateful for the opportunity to participate in this research experience funded by the National Science Foundation. Thank you to my mentors Dr. Giles Hammond and Dr. Alan Cumming who provided daily support through out my internship. Thank you to Mr. Karl Toland who's master thesis was a huge help in my research and who was able to provide necessary guidance during my internship. Thank you to Mr. Colin Craig and Mr. Russel Jones for designing and machining parts for the upgrade of the strength tester. Thank you to Stephen Craig for help in the electronics room. Thank you to the program coordinators at the University of Florida: Dr. Guido Mueller, Dr. Bernard Whiting, and Ms. Kristin Nichola. Thank you to all the other participants with the IREU program for comic relief and chat support via Facebook. Thank you to my mentor at Normandale Community College, Dr. Angela Foudray. Lastly, I would like to thank everyone within the IGR and Physics department at University of Glasgow.

References

[1] Albert Einstein. *Naherungsweise Integration der Feldgleichungen der Gravitation*, pages 99–108. Wiley-VCH Verlag GmbH & Co. KGaA, 1916. ISBN 9783527608959. doi: 10.1002/3527608958.ch7. URL http://dx.doi.org/10.1002/3527608958.ch7.

[2] James Overduin. Special & general relativity questions and answers what is a space time continuum?, 2010. URL https://einstein.stanford.edu/content/relativity/q411.html.

[3] R. M. Shannon, V. Ravi, L. T. Lentati, P. D. Lasky, G. Hobbs, M. Kerr, R. N. Manchester, W. A. Coles, Y. Levin, M. Bailes, N. D. R. Bhat, S. Burke-Spolaor, S. Dai, M. J. Keith, S. Osłowski, D. J. Reardon, W. van Straten, L. Toomey, J.-B. Wang, L. Wen, J. S. B. Wyithe, and X.-J. Zhu. Gravitational waves from binary supermassive black holes missing in pulsar observations. *Science*, 349(6255):1522–1525, 2015. ISSN 0036-8075. doi: 10.1126/science.aab1910. URL http://science.sciencemag.org/content/349/6255/1522.

[4] Karl William Toland. Development and characterisation of a pulling machine to produce small diameter silica fibres for use in prototype advanced gravitational wave detectors. Masters thesis, University of Glasgow, 2015.

[5] Kai Staats. Detecting ripples in space-time, with a little help from einstein, 2015. URL https://www.space.com/30203-observatory-to-spot-colliding-black-holes-in-space.html.

[6] Peter R. Saulson. Student, 1998. URL http://www2.astro.psu.edu/users/steinn/Astro597/saulson.pdf.

[7] IPAC Communications & Education Team. Ligo's interferometer, 2017. URL https://www.ligo.caltech.edu/page/ligos-ifo.

[8] B. P. Abbott, R. Abbott, T. D. Abbott, M. R. Abernathy, F. Acernese, K. Ackley, C. Adams, T. Adams, P. Addesso, R. X. Adhikari, V. B. Adya, C. Affeldt, M. Agathos, K. Agatsuma, N. Aggarwal, O. D. Aguiar, and et. al. Observation of gravitational waves from a binary black hole merger. *Phys. Rev. Lett.*, (116), 2016.

[9] Sheila Rowan and Jim Hough. Gravitational wave detection by interferometry (ground and space). *Living Reviews in Relativity*, 3(1):3, Jun 2000. ISSN 1433-8351. doi: 10.12942/lrr-2000-3. URL https://doi.org/10.12942/lrr-2000-3.

[10] Quasi-monolithic suspensions, 2017. URL http://www.physics.gla.ac.uk/igr/dev/igr/index.php?L1=research&L2=suspensions.

[11] Giles Hammond, S. Hild, and M. Pitkin. Advanced technologies for future ground-based, laser-interferometric gravitational wave detectors. *Journal of Modern Optics*, 61:S10–S45, 2014.

[12] A V Cumming, A S Bell, L Barsotti, M A Barton, G Cagnoli, D Cook, L Cunningham, M Evans, G D Hammond, G M Harry, A Heptonstall, J Hough, R Jones, R Kumar, R Mittleman, N A Robertson, S Rowan, B Shapiro, K A Strain, K Tokmakov, C Torrie, and A A van Veggel. Design and development of the advanced ligo monolithic fused silica suspension. *Classical and Quantum Gravity*, 29(3):035003, 2012. URL http://stacks.iop.org/0264-9381/29/i=3/a=035003.

[13] Chris J. Bell, Stuart Reid, James Faller, Giles D. Hammond, Jim Hough, Iain W. Martin, Sheila Rowan, and Kirill V. Tokmakov. Experimental results for nulling the effective thermal expansion coefficient of fused silica fibres under a static stress. *Classical and Quantum Gravity*, 31(6), 2014.

[14] Dr. RÃŒdiger Paschotta. Q factor in encyclopedia of laser physics and technology, 2008. URL https://www.rp-photonics.com/q_factor.html.

[15] S. D. Mescherlakov A. V. Dmitrie and and and V. P. Mitrofanov K. V. Tokmakov. Controllable damping of high-q violin modes in fused silica suspension bers. *Classical and Quantum Gravity*, 27:025009, 2010.

[16] S Gossler, G Cagnoli, D R M Crooks, H Luck, S Rowan, J R Smith, K A Strain, J Hough, and K Danzmann. Damping and tuning of the fibre violin modes in monolithic silica suspensions. *Classical and Quantum Gravity*, 21(5):S923, 2004. URL http://stacks.iop.org/0264-9381/21/i=5/a=082.

[17] Joe Wolfe. Young's modulus, hooke's law and material properties, 2017. URL http://www.animations.physics.unsw.edu.au/jw/elasticity.htm.

[18] The Editors of EncyclopÃŠdia Britannica. Young's modulus. *EncyclopÃŠdia Britannica, inc.*, 2016. URL https://www.britannica.com/science/Youngs-modulus.

[19] C.R. Nave. Young's modulus, 2017. URL http://hyperphysics.phy-astr.gsu.edu/hbase/permot3.html.

[20] Alastair W. Heptonstall. Characterization of mechanical loss in fused silica ribbons for use in gravitational wave detector suspensions, 2004.

[21] Gregor Taylor. The design of the mkiii igr strength testing unit, 2013.

[22] Russell Jones, Alastair Grant, Mark Barton, Angus Bell, Alan Cumming, Liam Cunningham, Giles Hammond, Alastair Heptonstall, Jim Hough, Rahul Kumar, Sheila Rowan, Ken Strain, Kirill Tokmakov, Calum Torrie, and Marielle van Veggel. The design of the igr mkii strength

testing machine (2008). Technical report, Institute for Gravitational Research, University of Glasgow, 2008.

[23] Magnetic sensor msk5000 linear, 2017. URL https://www.siko-global.com/en-us/products/magline-magnetic-linear-and-angular-measurement/magnetic-sensors/msk5000-linear.

[24] National Instruments. Usb-6008 12-bit, 10 ks/s low-cost multifunction daq, 2017. URL http://sine.ni.com/nips/cds/view/p/lang/en/nid/201986.

[25] Edwardson. Relay contact bounce test, 2011. URL http://electromotiveforces.blogspot.co.uk/2011/01/relay-contact-bounce-test.html.

[26] Dynapar. Quadrature encoder overview, 2007. URL http://www.dynapar.com/Technology/Encoder_Basics/Quadrature_Encoder/.

[27] Newport. High performance linear stage, 400 mm travel , linear motor, m6, 2017. URL https://www.newport.com/p/M-IMS400LM.

[28] Accuratus. Fused silica, sio2 glass properties, 2013. URL http://accuratus.com/fused.html.

A Appendix Calibration Graphs

Raw calibration data.

Notes	Round	Up/down	Start time	End Time	Steps	Start Caliper (mm)	End Caliper (mm)	Displacement (mm)	Encoder Count	MM/Count	Count/MM	mm/step
	1	up	11:46	11:51	2000	54.89	55.09	0.20	226	0.000885	1,130.00	0.0001
	2	up	11:51	11:53	2000	55.09	55.58	0.49	223	0.002197	455.10	0.000245
	3	up	11:54	11:56	2000	55.58	55.84	0.26	220	0.001182	846.15	0.00013
	4	up	11:57	11:58	2000	55.84	56.01	0.17	224	0.000759	1,317.65	0.000085
displacement measuremer	5	up	11:59	12:01	2000	56.01	55.99	0.02	221	0.000090	11,050.00	0.00001
	6	up	12:03	12:10	10000	55.99	57.34	1.35	1103	0.001224	817.04	0.000135
	7	up	12:11	12:19	10000	57.34	58.26	0.92	1095	0.000840	1,190.22	0.000092
	8	up	12:20	12:27	10000	58.26	59.3	1.04	1113	0.000934	1,070.19	0.000104
	9	up	13:01	13:10	10000	59.34	60.58	1.24	1113	0.001114	897.58	0.000124
	10	up	13:11	13:20	10000	60.58	61.83	1.25	1094	0.001143	875.20	0.000125
	11		13:20	13:29	10000	61.83	60.61	1.22	1017	0.001200	833.61	0.000122
	12		13:29	13:37	10000	60.61	59.34	1.27	1097	0.001158	863.78	0.000127
	13		13:38	13:46	10000	59.34	58.36	0.98	1107	0.000885	1,129.59	0.000098
	14		13:48	13:55	10000	58.36	57.11	1.25	1116	0.001120	892.80	0.000125
	15		14:06	4:17	10000	57.11	55.06	2.05	1089	0.001882	531.22	0.000205
	16		14:18	14:24	10000	55.06	53.92	1.14	1112	0.001025	975.44	0.000114
									Average	0.001102439879	1,554.72	0.0001213125

B Appendix LabVIEW

Block diagram for the original Stepper_2 program.

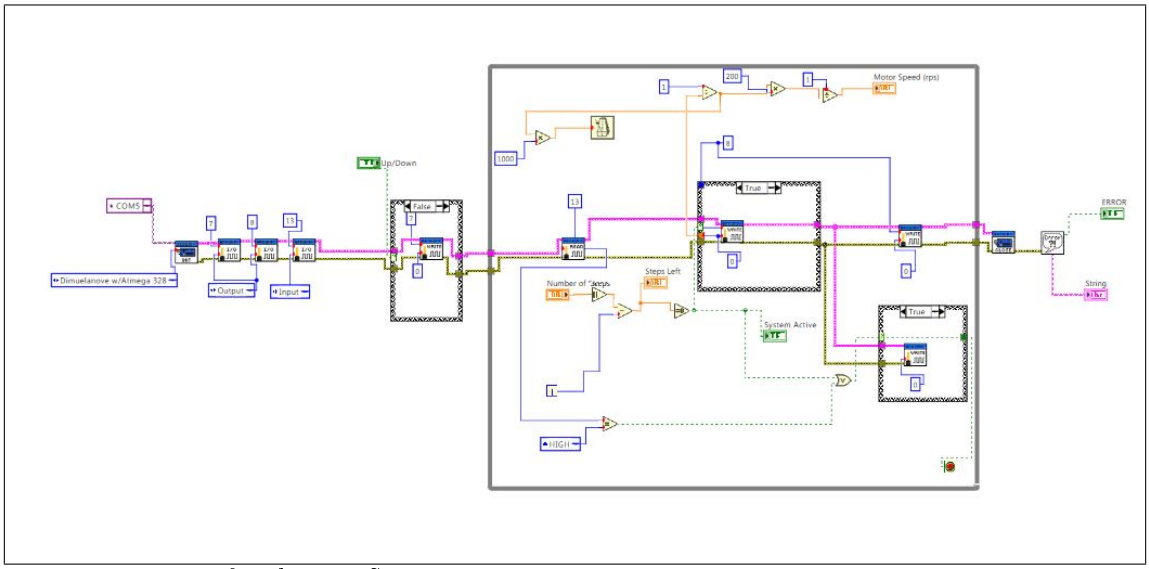

Block Diagram for the new Stepper3_V5 program, Image 1

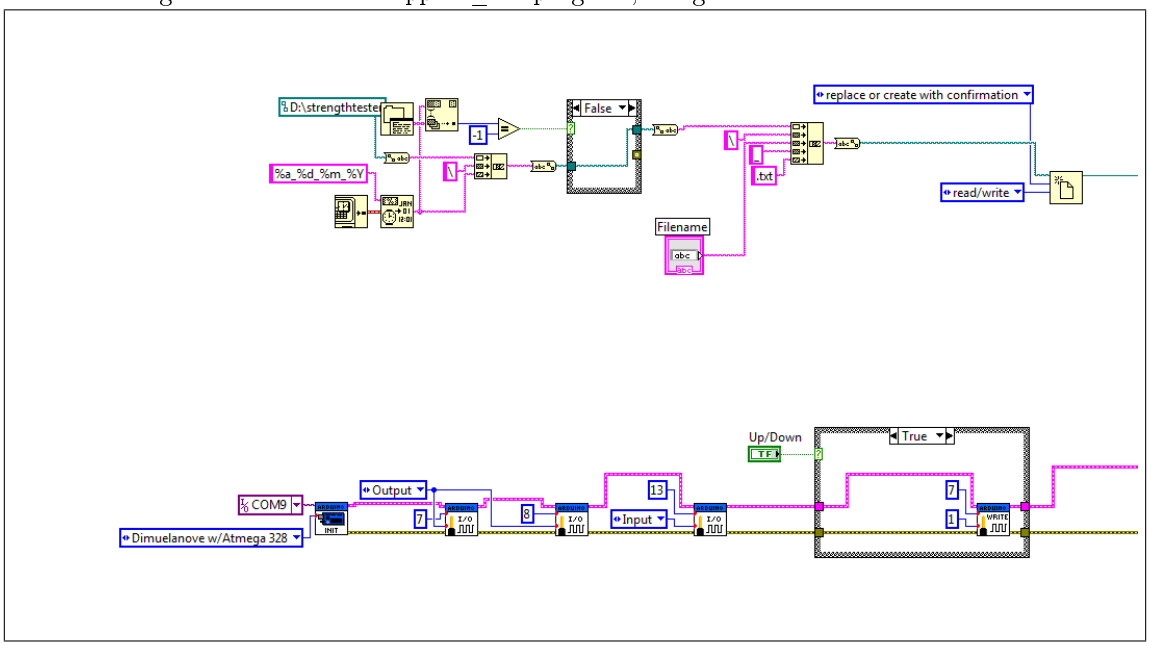

Image 2

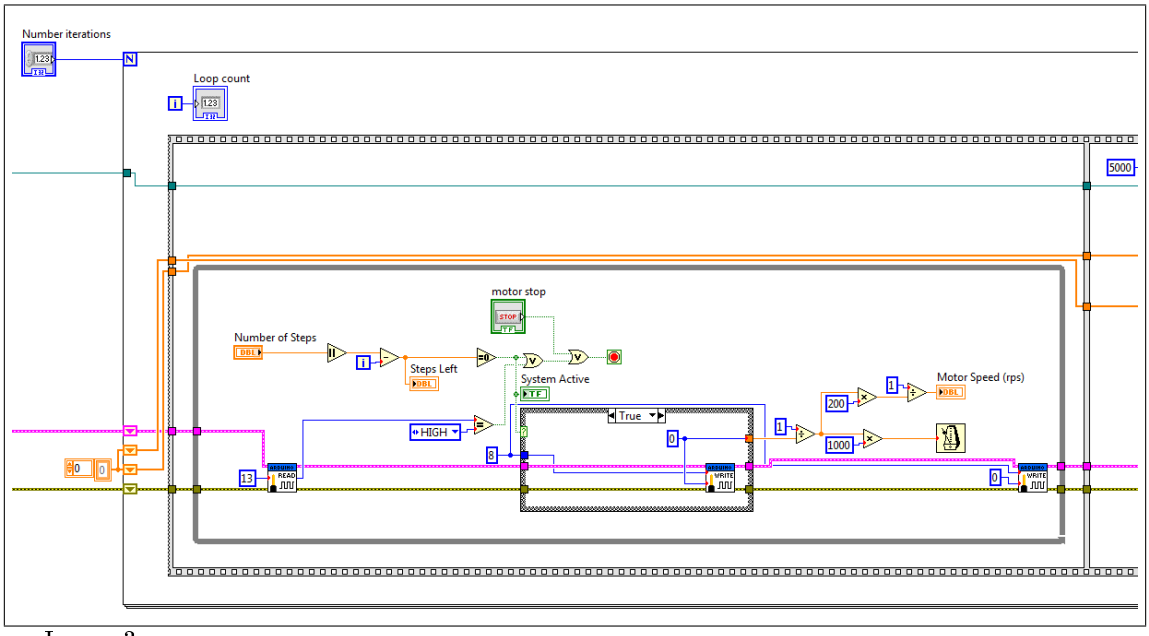
Number iterations
Loop count
5000
motor stop
Number of Steps
Steps Left
System Active
HIGH
True
200
1000
Motor Speed (rps)

Image 3

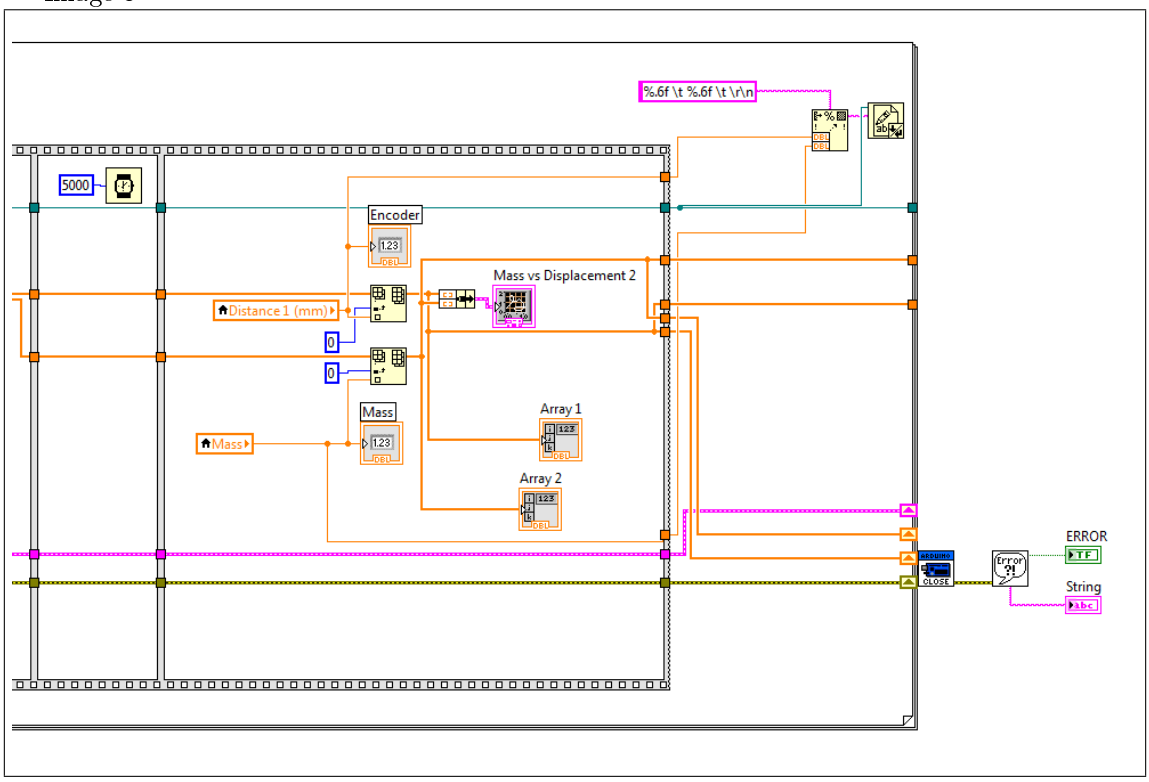
%.6f \t %.6f \t \r\n
5000
Encoder
Mass vs Displacement 2
Distance 1 (mm)
Mass
Array 1
Array 2
ERROR
String